



PONTIFICIA UNIVERSIDAD CATÓLICA DE CHILE
ESCUELA DE INGENIERÍA

ON VARIATIONAL FORMULATIONS OF PRESSURE-DRIVEN POROMECHANICS

FELIPE ÁLVAREZ BARRIENTOS

Thesis submitted to the Office of Research and Graduate Studies
in partial fulfillment of the requirements for the degree of
Master of Science in Engineering

Advisor:

DANIEL HURTADO

Santiago de Chile, March 2021

© 2021, FELIPE ÁLVAREZ BARRIENTOS



PONTIFICIA UNIVERSIDAD CATÓLICA DE CHILE
ESCUELA DE INGENIERÍA

ON VARIATIONAL FORMULATIONS OF PRESSURE-DRIVEN POROMECHANICS

FELIPE ÁLVAREZ BARRIENTOS

Members of the Committee:

DANIEL HURTADO

DIEGO CELENTANO

MARTIN GENET

LEONARDO VANZI

Thesis submitted to the Office of Research and Graduate Studies
in partial fulfillment of the requirements for the degree of
Master of Science in Engineering

Santiago de Chile, March 2021

© 2021, FELIPE ÁLVAREZ BARRIENTOS

*To my parents,
Mariana and Fernando*

ACKNOWLEDGEMENTS

I would like to thank Daniel Hurtado and Martin Genet, who have guided me in the development of this thesis. Over the past two years, our periodic meetings have shown me how important collaboration is for science, and how sharing different perspectives and questioning the models and results we obtain, are the key to extend the barriers of knowledge. I also wish to thank the committee members, Diego Celentano and Leonardo Vanzi, for their time and comments about this thesis.

During this period, my partners of the CB2L laboratory have helped me considerably; I appreciate their company, the fruitful discussions and the kind moments we shared. I also wish to thank MΞDISIM's members, who made my stays in France very pleasant, from a scientific and a personal perspective.

In school, and later in university, I made friends with whom I have had the opportunity to share the beautiful, and sometimes hard, moments of life. I know many of them since before I can remember, and having the possibility of learning with (and from) them, has made me a better person. Specially thanks to them for their company, for supporting me when I needed it, and in the last months, for always patiently listening to me talk about this thesis.

Finally, I would like to thank my family, especially my parents, Mariana and Fernando, who always have supported and accompanied me. This work is dedicated to you; your inspiration and support have created in me the curiosity and passion for learning more, and the confidence to pursue my dreams.

TABLE OF CONTENTS

ACKNOWLEDGEMENTS	iv
LIST OF FIGURES	vii
ABSTRACT	viii
RESUMEN	ix
1. INTRODUCTION	1
1.1. Motivation	1
1.2. Microstructure in the mechanics of porous materials	2
1.3. Continuum Mechanics Theory	5
1.3.1. Kinematics	6
1.3.2. Constitutive laws and stress measures	7
1.3.3. Equilibrium	8
1.3.4. Mixed formulation for incompressibility	11
1.3.5. Decomposition of the displacement and kinematical constraints	14
1.4. Thesis Structure	16
2. PRESSURE-DRIVEN MICRO-PORO-MECHANICS: A VARIATIONAL FRAMEWORK FOR MODELING THE RESPONSE OF POROUS MATERIALS	17
2.1. Introduction	17
2.2. Micromechanical Model: Variational Framework	20
2.2.1. Kinematical constraints	25
2.3. Numerical Examples	28
2.3.1. Spherical alveolar model	29
2.3.2. Image-based alveolar model	32
2.4. Discussion	35

Acknowledgements	39
3. CONCLUSIONS	40
4. PERSPECTIVES	41
BIBLIOGRAPHY	42
APPENDICES	53
A. Balance of angular momentum and symmetry of \bar{U}	54
B. Micromechanical analysis including body force	57
C. Macroscopic averaged response	62

LIST OF FIGURES

1.1	Examples of open-cell and closed-cell foams.	2
1.2	RVE of lung parenchyma obtained using micro-CT.	4
1.3	2D schematic of a closed-cell foam RVE.	12
1.4	Decomposition of the displacement.	13
1.5	2D schematic of a periodic RVE.	15
2.1	Schematic of a periodic foam-like material RVE and meshes of the spherical and image-based alveolar models.	22
2.2	Hydrostatic stress field in the spherical alveolar model.	31
2.3	Von Mises stress field in the spherical alveolar model.	31
2.4	Hydrostatic and von Mises stress distributions for the spherical alveolar model.	32
2.5	Reflection of the image-based mesh.	33
2.6	Hydrostatic stress field in the image-based alveolar model.	34
2.7	Von Mises stress field in the image-based alveolar model.	34
2.8	Hydrostatic and von Mises stress distributions for the image-based alveolar model.	35
2.9	Comparison of the hydrostatic and von Mises stress distributions for the pressure-driven RVE, with the spherical and image-based alveolar models. . .	37
C.1	Determinant of \mathbf{F}^c for the spherical and image-based alveolar models.	63
C.2	Hydrostatic and von Mises components of the macroscopic Cauchy stress for the spherical and image-based alveolar models.	63

ABSTRACT

Porous materials are solids containing void spaces, and their arrangement at the microscopic level confers them unique properties, with practical applications in areas such as civil engineering and medicine. To understand these materials' behavior, diverse micromechanical models have been proposed, in which typically there are prescribed displacements or simple loading states, such as uniaxial compression or simple shear. However, the case of micromechanical models of porous materials where the pore pressure produces the deformation, here denominated pressure-driven models, has been understudied, and it is the focus of this thesis. In this work, we develop a finite-deformation variational framework for pressure-driven foams, which allows for various boundary conditions: kinematic uniform displacements, periodic displacements, and uniform traction. Then, we apply the model in numerical simulations in the context of lung micromechanics, first with a spherical alveolar model and then with an image-based alveolar model. The results show that the stress distributions are different for each kinematical constraint in the spherical model, while in the image-based model, the distributions are independent of the constraints. Besides, we compare the pressure-driven and deformation-driven models, obtaining that between both cases, the hydrostatic stress distributions are shifted, while the deviatoric stresses are the same. Interestingly, the pressure-driven and deformation-driven simulations of the lung parenchyma can be related to mechanical ventilation and spontaneous breathing, respectively, and the results obtained give an insight into the differences between both states.

Keywords: Open-cell Foam Material, Micromechanics of Porous Materials, Lung Mechanics, Poromechanics, Pressure-driven Models.

RESUMEN

Los materiales porosos son sólidos que contienen cavidades en su interior, y su distribución a nivel microscópico les confiere propiedades únicas, con aplicaciones prácticas en áreas como ingeniería civil y medicina, entre otras. Para entender el comportamiento de estos materiales, diversos modelos micromecánicos han sido propuestos, en los cuales típicamente existen desplazamientos prescritos o condiciones de carga simples, como compresión uniaxial o corte simple. Sin embargo, el caso de modelos micromecánicos de materiales porosos en donde la presión produce la deformación ha sido poco estudiado, y es precisamente el foco de esta tesis. Para lograr esto, desarrollamos una formulación variacional en deformaciones finitas para materiales porosos, en donde la presión produce la deformación, y que además permite varias condiciones de borde: desplazamientos uniformes, desplazamientos periódicos y tracción uniforme. Luego, aplicamos el modelo en simulaciones numéricas de tejido pulmonar, primero con un modelo alveolar esférico, y luego con un modelo alveolar basado en imágenes. Los resultados muestran que para el modelo esférico las distribuciones de tensión son diferentes para cada restricción cinemática, mientras que en el modelo basado en imágenes las distribuciones obtenidas son independientes de la restricción utilizada. Además, comparamos los modelos impulsados con presión con modelos con deformaciones prescritas equivalentes, obteniendo que entre ambos casos la tensión hidrostática experimenta un desplazamiento de sus valores, manteniendo la forma de la distribución, mientras que la tensión de von Mises no se ve afectada. De forma interesante, los modelos impulsados por presión y con deformaciones prescritas pueden ser relacionados con ventilación mecánica y respiración espontánea, respectivamente, y los resultados obtenidos ayudan a entender las diferencias entre ambos estados.

Palabras clave: Materiales porosos con celdas abiertas, Análisis micromecánico de materiales porosos, Mecánica pulmonar, Poromecánica, Modelos impulsados por presión.

1. INTRODUCTION

1.1. Motivation

Porous materials can be defined as solids containing fluid-filled space(s), and they are ubiquitous in nature, with examples as varied as saturated rocks, wood, coral, plant cells, and biological tissues. Throughout history, human beings have made use of them, from civil engineering applications to everyday use, as in ingenious wooden artifacts in the construction of the Egyptian pyramids, or simply cork, used since Roman times to stopper wine bottles (Gibson & Ashby, 1997). More recently, the properties of this kind of materials have motivated the development of new technologies to create them artificially, so they can be used for isolation, cushioning, and absorption of energy from impacts, among others. Their outstanding properties and multiple applications have driven the study of their microscopic features, revealing a link between their global (or macroscopic) behavior and the underlying microstructure.

In porous materials, the microstructure plays a key role, which affects not only local mechanisms but also the material's global behavior. At the microstructural level, the cavities allow the classification of these materials as closed-cell (CCF) or open-cell (OCF) foams; the former are defined as materials with isolated cavities embedded in it, while in the latter these are interconnected (Gibson & Ashby, 1997; Ma et al., 2011), as shown in Figure 1.1. Furthermore, the microstructural arrangement in CCFs and OCFs strongly influences the mechanical response, which is dominated by mechanisms such as bending of struts, buckling of cell walls, the formation of yield joints or folds, and fracture of cell struts and cell walls (Altenbach & Öchsner, 2010; Deville et al., 2006; Genet et al., 2014; Houmard et al., 2013). In this type of materials, cavities can be subject to the pressure exerted by a fluid or gas. Examples of pressurized materials are the foams used to thermally insulate the Space Shuttle external tank (Bednarczyk et al., 2008), where thermoelastic and thermoinelastic effects are also present, the lung parenchyma, where the air entering in the respiratory system produces the inner pressure (Koshiyama et al., 2019; Patte et al.,

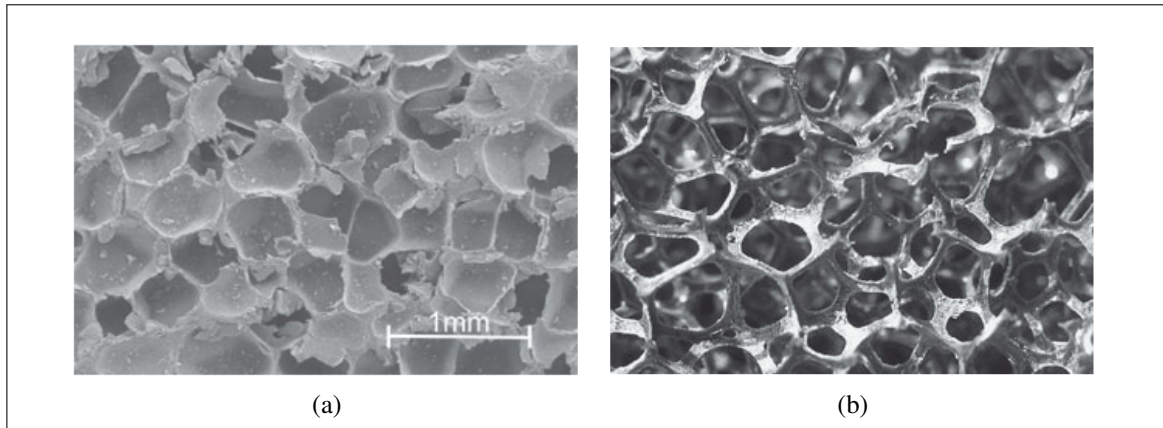


Figure 1.1. Examples of polymeric foams, with (a) closed-cells and (b) open-cells. Taken from Altenbach and Öchsner (2010).

2021; Rausch et al., 2011; Sarabia-Vallejos et al., 2019), and porous elastomers, where the presence of pressurized cavities has proven to affect the overall response, producing, for instance, the shrinkage of elastomeric foams after demolding (Fen-Chong et al., 1999; Idiart & Lopez-Pamies, 2012). Therefore, it is relevant to study the mechanical response of porous materials with models that consider the microscopic properties, as the structural arrangement, the presence (or not) of pressure in the cavities, and the solid skeleton behavior.

Given the key-role of the microstructure in porous materials, this thesis's objective is to develop a variational framework for the micromechanical analysis of CCFs and OCFs, which will be tested in numerical examples using the Finite Element Method (FEM). In particular, the variational framework will address the case of the micromechanical response of pressurized foams, where the deformation is driven by the pore pressure of the fluid in the cavities.

1.2. Microstructure in the mechanics of porous materials

Since the microstructure of porous materials (and in a general manner, of all kinds of materials) is relevant in the context of mechanical models, several approaches have been

proposed to perform simulations across the scales, i.e., obtaining a global response that is influenced by the heterogeneities present at the microscale. A first direct but inefficient method is to perform a simulation of the entire body, including all heterogeneities. Since this approach directly incorporates all the information of the problem (geometry, boundary conditions, microscopic properties), it is quite redundant and in practice unfeasible due to its high computational cost and memory storage requirements. To solve this issue, multiscale models based on homogenization theory have been developed in the last decades. In the homogenization method, given that the lengths scales of the micro- and macro-problems are sufficiently separated, the main objective is to estimate the effective macroscopic properties of an heterogeneous material, so it can be substituted with an equivalent homogeneous one (Saeb et al., 2016). The microstructure's influence is reflected in the effective properties; hence, the model does not need to incorporate the heterogeneities directly, and the computational cost is reduced considerably. One of the most common homogenization techniques is based on variational principles and asymptotic expansions of strain and stress fields, which lead to a set of boundary value problems at the micro- and macroscale (Saeb et al., 2016). Since the pioneering works of Hill (1972) and Ogden (1974), who extended analytical homogenization to nonlinear composites and finite deformation elasticity, many researchers have contributed to the development and application of this techniques (Bakhvalov & Panasenko, 1989; Fish, 2013; Hashin, 1983; Hollister & Kikuchi, 1992; Huet, 1990; Ponte Castañeda, 1991; Sanchez-Palencia, 1980; Suquet, 1987; Willis, 1981), which are still used in diverse fields.

The homogenization models have proven to be an effective way to predict the macroscopic response of materials. However, its application to real 3D microstructures is limited, due to the assumptions of idealized microstructures and boundary conditions in which they are based (Cao et al., 2014; Hannard et al., 2016; Shakoor et al., 2017). To address this issue, numerical simulations have been conducted in the microscale, where the mechanical problem is stated on a representative volume element (RVE) of the material's underlying microstructure. In order to preserve the microstructure of the material, the RVE can be obtained by micro-computed tomography (micro-CT) (Bargmann et al., 2018), as seen,

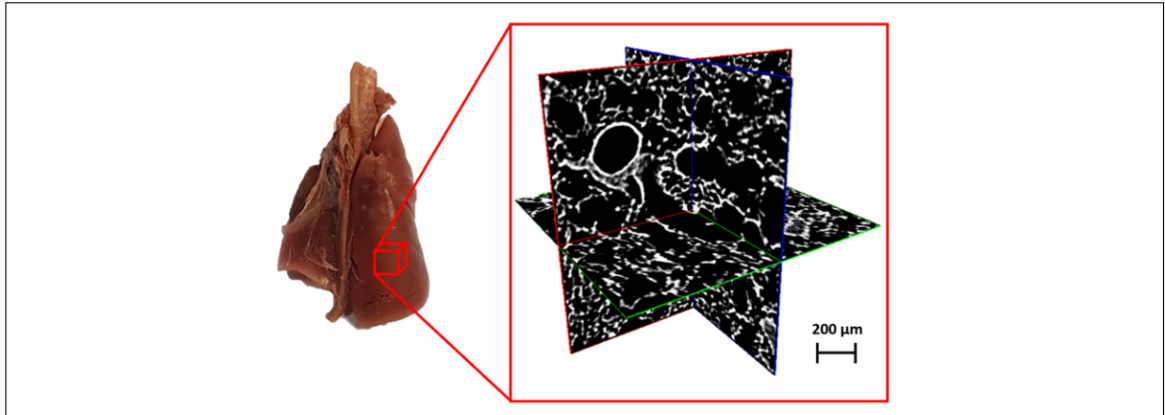


Figure 1.2. The micromechanical problem is solved in an RVE of the material. In the figure, an RVE of lung parenchyma is selected from micro-CT images of the whole-lung. Taken from Sarabia-Vallejos et al. (2019).

for instance, in Figure 1.2 for the lung parenchyma. Then, the microstructural problem is solved to obtain the stress and strain distributions within the RVE. Note that although this approach omits the macroscopic information (as the geometry and boundary conditions of the whole body), it allows to obtain information about local mechanisms, as stress hotspots or relations between global and local strain (Kantzios et al., 2018; Rausch et al., 2011).

The cavities in porous materials may contain fluid, and according to the assumptions on the fluid response, different models have been proposed. If the fluid's motion is being modeled, the Navier-Stokes equations or Darcy's law can be considered (Collis et al., 2017; Selvadurai & Suvorov, 2016), which can be used to study the flow through porous materials. The models that consider the fluid dynamics give more information about the mechanics but increase the mathematical complexity and incorporate new variables, leading to higher computational cost. So, if the focus is on the solid skeleton behavior and dynamic effects can be neglected, certain models only incorporate the pressure of the fluid (Idiart & Lopez-Pamies, 2012; Ma et al., 2011; Sarabia-Vallejos et al., 2019), which can be used to analyze the effects of having pressurized versus vacuum cavities and how this affects the overall response of the body, for example. Following this approach, in this work the effects related to the fluid dynamics will be neglected, incorporating in the model only

the pressure of the fluid, which will have a fundamental role in the deformation of the RVE, as discussed next.

So far, it has been established that in order to preserve the microstructure of the material, RVEs can be constructed from micro-CT images. Additionally, to state the mechanical problem, it is necessary to determine the loading of the RVE. The case where the loading conditions are based on a given macroscopic strain, or stress, has been widely studied, both theoretically (De Souza Neto & Feijóo, 2006; Dormieux et al., 2002) and in numerical simulations (Liu & Chen, 2015; Ma & Yang, 2018). The values for the given quantities may come from multiscale analysis or represent arbitrary states, depending on the study's scope. Conversely, the case where the pore pressure drives the deformation in the RVE, and the macroscopic strain and stress are variables of the problem, has been understudied, and only by numerical methods, with a theoretical framework still missing. In the next section, the basis for solving the pressure-driven problem will be set, which consists of the continuum mechanics theory, which has been widely used in the context of finite deformations.

1.3. Continuum Mechanics Theory

The formulation of continuum mechanics dates back to the 18th century and required the efforts of renowned scientists, who laid its foundations and presented them in elegant mathematical terms. In 1687 Isaac Newton (1642-1727) published “Principia”, which contains Newton’s laws of motion and the law of gravitational attraction. Then, to extend the laws of motion from a system of particles to the differential equations for a continuous medium, it was necessary the interventions of figures such as the Bernoullis (John, James, and Daniel), Leibniz, Euler, d’Alembert, Coulomb and Lagrange. In 1788, 101 years after the publication of Newton’s “Principia”, Lagrange published “Mécanique Analytique”, which unified the progress made and presented the formulation of mechanical problems in terms of differential equations. Then, from 1823 to 1841, Augustin-Louis Cauchy (1789-1857) developed almost entirely the finite-strain theory and introduced the general concept

and mathematical theory of the stress tensor (Soutas-Little, 2009; Tadmor et al., 2012). From that point, several contributors have applied and extended the continuum mechanics theory, relating it with the thermodynamic's laws, non-linear materials, viscoelasticity, among many other subjects.

1.3.1. Kinematics

To formulate the continuum mechanics theory in the context of porous materials, first some definitions must be presented. Let Ω_0 be the reference (or material) configuration, which represents the state where no external loading is applied to the body (Tadmor et al., 2012); and let \mathbf{X} be the position of a particle in the reference configuration. Then, the deformed (or spatial) configuration Ω can be described in terms of a one-to-one deformation mapping function φ that maps the reference position of every particle of the body $\mathbf{X} \in \Omega_0$ to its deformed position $\mathbf{x} \in \Omega$, such that $\mathbf{x} = \varphi(\mathbf{X})$. Then, the displacement field is defined as $\mathbf{u}(\mathbf{X}) := \varphi(\mathbf{X}) - \mathbf{X}$. With \mathbf{X} and \mathbf{x} defined, the deformation gradient tensor \mathbf{F} is expressed as

$$\mathbf{F}(\mathbf{X}) := \frac{\partial \varphi}{\partial \mathbf{X}}(\mathbf{X}) = \frac{\partial \mathbf{x}}{\partial \mathbf{X}} = \nabla_0 \mathbf{x}. \quad (1.1)$$

The jacobian of $\mathbf{F}(\mathbf{X})$ provides a local measure for volume changes, and it is defined as

$$J(\mathbf{X}) := \det \mathbf{F}(\mathbf{X}) > 0. \quad (1.2)$$

Since $\mathbf{F}(\mathbf{X})$ is invertible, $J(\mathbf{X}) \neq 0$, and as volume elements cannot have negative volumes, $J(\mathbf{X}) < 0$ is not physically possible, which justifies the last relation in Equation (1.2). The jacobian $J(\mathbf{X})$ can also be understood as a relation between infinitesimal volume elements, defined in the reference (dV) and current (dv) configurations (Holzapfel, 2000),

$$dv = J(\mathbf{X})dV. \quad (1.3)$$

The deformation gradient tensor $\mathbf{F}(\mathbf{X})$ has information not only about the stretch and shear of the neighborhood of a material particle from the reference to deformed configurations, but also about rotations. However, it can be decomposed uniquely into a pure stretch (and shear) tensor and a pure rotation tensor, according to the polar decomposition theorem: any tensor \mathbf{F} with positive determinant ($\det \mathbf{F} > 0$) can be uniquely expressed as

$$\mathbf{F} = \mathbf{R}\mathbf{U} = \mathbf{V}\mathbf{R}, \quad (1.4)$$

called the right and left polar decompositions of \mathbf{F} , where \mathbf{R} is a proper orthogonal transformation, which represents a finite rotation, and \mathbf{U} and \mathbf{V} are the symmetric positive-definite right and left stretch tensors, respectively (Tadmor et al., 2012).

1.3.2. Constitutive laws and stress measures

In mechanics, the behavior of different kinds of materials is represented by constitutive laws. To achieve that, constitutive equations are used, which are functional relationships that model the behavior of materials, establishing a connection between stress and other fields of interest, such as strain and temperature (Holzapfel, 2000). In this thesis, hyperelastic materials will be studied, which do not have a viscous (or dissipative) behavior, and for which there exist a Helmholtz free-energy function ψ , also known as strain energy density function (SEF) when $\psi = \psi(\mathbf{F})$. Then, the stress is given by the derivative of the SEF with respect to strain

$$\mathbf{P}(\mathbf{F}) = \frac{\partial \psi}{\partial \mathbf{F}}(\mathbf{F}), \quad (1.5)$$

where $\mathbf{P}(\mathbf{X})$ is the first Piola-Kirchhoff stress tensor (which corresponds to the engineering or nominal stress, the force per unit area in the reference configuration). The Cauchy stress tensor is a measure of the true stress, the force per unit area in the deformed configuration, and is related to the first Piola-Kirchhoff stress tensor \mathbf{P}^1 by the relation $\boldsymbol{\sigma} = J^{-1} \mathbf{P} \mathbf{F}^T$, hence

$$\boldsymbol{\sigma} = J^{-1} \frac{\partial \psi}{\partial \mathbf{F}}(\mathbf{F}) \mathbf{F}^T. \quad (1.6)$$

¹For clarity, the dependency of $\mathbf{P}(\mathbf{F})$, $\mathbf{S}(\mathbf{F})$, $\boldsymbol{\sigma}(\mathbf{F})$, $\mathbf{F}(\mathbf{X})$, $\mathbf{u}(\mathbf{X})$, $J(\mathbf{X})$ on \mathbf{F} and \mathbf{X} will be omitted.

Another stress measure is the second Piola-Kirchhoff stress tensor \mathbf{S}

$$\mathbf{S} = \mathbf{F}^{-1} \mathbf{P}, \quad (1.7)$$

and note that, contrary to \mathbf{P} , $\boldsymbol{\sigma}$ and \mathbf{S} are symmetric tensors. Both \mathbf{P} and \mathbf{S} are suitable when the problem is formulated in the reference configuration, while $\boldsymbol{\sigma}$ is used when the deformed configuration is selected.

1.3.3. Equilibrium

Now, the equilibrium will be expressed in terms of the principle of stationary potential energy. To establish this variational principle, we assume the existence of an energy functional, that for continuum mechanics problems is the total potential energy Π_{tot} , defined as the strain energy stored in the body plus the potential energy of external forces

$$\Pi_{\text{tot}}(\mathbf{u}) := \Pi_{\text{int}}(\mathbf{u}) + \Pi_{\text{ext}}(\mathbf{u}). \quad (1.8)$$

The potential energy stored in the body is

$$\Pi_{\text{int}}(\mathbf{u}) := \int_{\Omega_0} \psi(\mathbf{F}) dV, \quad (1.9)$$

while, as its name indicates, the potential energy of external forces Π_{ext} gathers the effect of the different external forces, such as body force, prescribed traction, or pressure, among others. For example, for the typical case of gravity loading

$$\Pi_{\text{ext}}(\mathbf{u}) = - \int_{\Omega_0} \rho_0 \mathbf{g} \cdot \mathbf{u} dV, \quad (1.10)$$

where ρ_0 is the density of the solid in the reference configuration, and \mathbf{g} is the gravitational acceleration.

Here, the variational problem has been formulated in terms of the displacement field \mathbf{u} (but it could also be developed in terms of the deformation mapping φ), and a displacement that satisfies the Dirichlet boundary conditions (which impose a given value for the displacement in a region of the boundary) is called admissible. With these definitions,

the principle of stationary potential energy is stated as: given the set of admissible displacement fields for a conservative system, an equilibrium state will correspond to one for which the total potential energy is stationary (Tadmor et al., 2012). Mathematically, if the potential energy is stationary at \mathbf{u}^* , this means

$$D_{\delta\mathbf{u}}\Pi_{\text{tot}}(\mathbf{u}^*) := \left. \frac{d}{d\eta}\Pi_{\text{tot}}[\mathbf{u}^* + \eta\delta\mathbf{u}] \right|_{\eta=0} = 0 \quad \forall \delta\mathbf{u}, \quad (1.11)$$

where $\delta\mathbf{u}$ is a small displacement field with $\delta\mathbf{u} = 0$ on the boundaries with Dirichlet conditions, so that $\mathbf{u}^* + \eta\delta\mathbf{u}$ is kinematically admissible. Further manipulations show that from (1.11) the differential equilibrium equations can be obtained (Holzapfel, 2000; Tadmor et al., 2012).

Special attention is needed if there is an external force depending on the displacement, for example, the pressure applied by a fluid. In the present work, this case is of particular relevance because in porous materials the presence of fluid in the cavities produces a pressure that is directly applied in the solid skeleton. Here, it will be mentioned the case of pore pressure in closed cavities, and in Chapter 2, it will be detailed for the case of pressure-driven RVEs of OCFs. Let p_0 be the pore pressure produced by the fluid and $\partial\Omega^N$ the deformed inner boundary (where the solid is in contact with the fluid). From the perspective of the solid, the pore pressure is exerted in $\partial\Omega^N$ with a traction vector $\mathbf{t} = -p_0\mathbf{n}$, which in terms of the virtual work corresponds to

$$\delta W_{\text{ext}}^p(\mathbf{u}, \delta\mathbf{u}) := - \int_{\partial\Omega^N} p_0\mathbf{n} \cdot \delta\mathbf{u} \, ds, \quad (1.12)$$

with \mathbf{n} the normal in the deformed configuration. However, as the inner boundary and the direction of the traction are displacement-dependent, the existence of a potential that could be included in the potential energy is not trivial. One of the cases where the pressure has an associated potential occurs if the surface where the pressure is applied encloses a certain region (Bonet & Wood, 1997). Let assume the cavities occupy a domain Ω_0^F in the reference configuration that is enclosed by a region $\partial\Omega_0^F$ (think, for example, in an RVE consisting in a central cavity surrounded by the solid skeleton, as depicted in Figure 1.3);

equivalently Ω^F and $\partial\Omega^F$ represent these regions in the deformed configuration. Then, the associated potential is

$$\Pi_{\text{ext}}^p(\mathbf{u}) := -p_0 \int_{\Omega^F} dv = -p_0 \int_{\Omega_0^F} J dV, \quad (1.13)$$

whose variation recovers the expression given by the external virtual work $\delta W_{\text{ext}}^p(\mathbf{u}, \delta\mathbf{u})$, as shown next. First, note that the derivative of Equation (1.13) is

$$\begin{aligned} D_{\delta\mathbf{u}}\Pi_{\text{ext}}^p(\mathbf{u}) &= -p_0 \int_{\Omega_0^F} J\mathbf{F}^{-T} : \nabla_0 \delta\mathbf{u} dV = -p_0 \int_{\Omega_0^F} JF_{ij}^{-T} \delta u_{i,j} dV \\ &= -p_0 \int_{\Omega_0^F} [(JF_{ij}^{-T} \delta u_i)_{,j} - (JF_{ij}^{-T})_{,j} \delta u_i] dV \\ &= -p_0 \left[\int_{\partial\Omega_0^F} J\mathbf{F}^{-T} \mathbf{N} \cdot \delta\mathbf{u} dS - \int_{\Omega_0^F} \nabla_0 \cdot (J\mathbf{F}^{-T}) \cdot \delta\mathbf{u} dV \right], \end{aligned} \quad (1.14)$$

where indicial notation (or Einstein notation) was used to make the derivation clearer, and \mathbf{N} is the normal in the reference configuration. The last expression can be simplified using the Piola identity

$$\nabla_0 \cdot (J\mathbf{F}^{-T}) = \mathbf{0}. \quad (1.15)$$

Here it will be shown a classical geometric derivation of this identity (Holzapfel, 2000, p. 146), for an analytical derivation note that $J\mathbf{F}^{-T} = \text{cof } \mathbf{F}$ and refer to Evans (1998, Ch. 8.1.4.b). First, let \mathcal{B}_0 be any region of a continuous body in the reference configuration, with boundary $\partial\mathcal{B}_0$; and let \mathcal{B} and $\partial\mathcal{B}$ be their counterparts in the current configuration. Then, using the divergence theorem and Nanson's formula $\mathbf{n} ds = J\mathbf{F}^{-T} \mathbf{N} dS$

$$\int_{\mathcal{B}_0} \nabla_0 \cdot (J\mathbf{F}^{-T}) dV = \int_{\partial\mathcal{B}_0} J\mathbf{F}^{-T} \mathbf{N} dS = \int_{\partial\mathcal{B}} \mathbf{n} ds \quad (1.16)$$

$$= \int_{\partial\mathcal{B}} \mathbf{I} \mathbf{n} ds = \int_{\mathcal{B}} \nabla \cdot \mathbf{I} dv = \mathbf{0}. \quad (1.17)$$

Then, using Piola identity in Equation (1.14)

$$D_{\delta\mathbf{u}}\Pi_{\text{ext}}^p(\mathbf{u}) = -p_0 \int_{\partial\Omega_0^F} J\mathbf{F}^{-T} \mathbf{N} \cdot \delta\mathbf{u} dS, \quad (1.18)$$

which is expressed in the reference configuration, contrary to $\delta W_{\text{ext}}^p(\mathbf{u}, \delta \mathbf{u})$, that is in the deformed configuration. However, using Nanson's formula, Equation (1.18) can be rewritten as

$$D_{\delta \mathbf{u}} \Pi_{\text{ext}}^p(\mathbf{u}) = -p_0 \int_{\partial \Omega^F} \mathbf{n} \cdot \delta \mathbf{u} \, ds = p_0 \int_{\partial \Omega^N} \mathbf{n} \cdot \delta \mathbf{u} \, ds, \quad (1.19)$$

where the sign changed because, although the boundary of the fluid domain $\partial \Omega^F$ is also the inner boundary of the solid $\partial \Omega^N$ (see Figure 1.3), the normals with respect to the fluid and the solid are opposite. Therefore, under the assumption of a closed cavity, the variation of the potential $\Pi_{\text{ext}}^p(\mathbf{u})$, given by Equation (1.19), recovers the expression of the virtual work $\delta W_{\text{ext}}^p(\mathbf{u}, \delta \mathbf{u})$ (the change in the sign is produced by the minus in the principle of virtual work: $\delta W_{\text{int}} - \delta W_{\text{ext}} = 0$, for vanishing accelerations).

1.3.4. Mixed formulation for incompressibility

As mentioned, the internal potential energy corresponds to the integral of the strain energy function; however, to model incompressible materials (which keep the volume constant throughout a motion), a mixed formulation can be adopted. First, note that the incompressibility constraint can be expressed as $J = 1$, which is included into the SEF of the material by using a Lagrange multiplier p

$$\psi(\mathbf{F}, p) = \psi_{\text{iso}}(\mathbf{F}) - p(J - 1), \quad (1.20)$$

where $\psi_{\text{iso}}(\mathbf{F})$ characterizes the isochoric response, and p corresponds to the hydrostatic pressure (Holzapfel, 2000). Following Equation (1.5), the first Piola-Kirchhoff stress tensor, in this case denoted as $\bar{\mathbf{P}}$, corresponds to

$$\bar{\mathbf{P}}(\mathbf{F}, p) = \frac{\partial \psi_{\text{iso}}}{\partial \mathbf{F}}(\mathbf{F}) - pJ\mathbf{F}^{-T}. \quad (1.21)$$

To summarize the contents exposed, below is shown the formulation for the case of an RVE consisting of an incompressible solid matrix with a pressurized interior cavity (that could represent a CCF). Let Ω_0^S and Ω_0^F be the solid and fluid domain in the reference

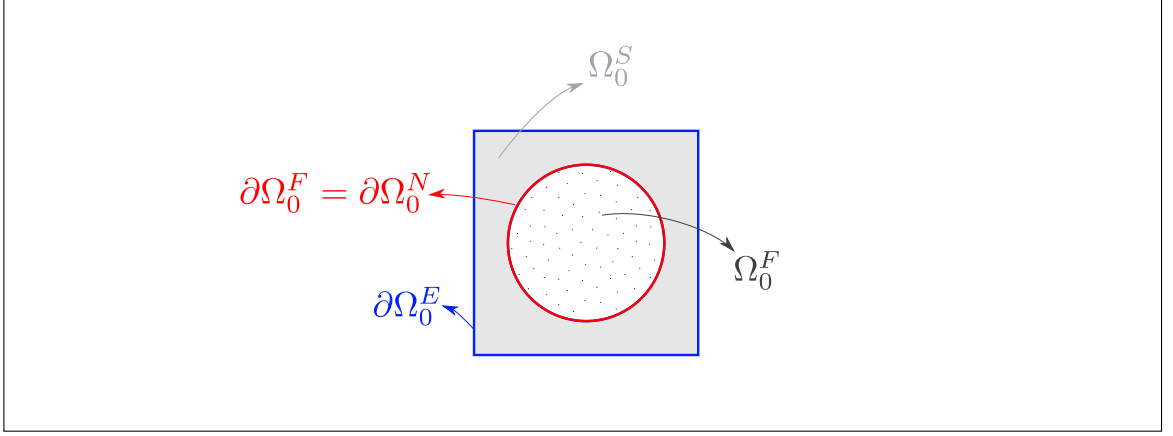


Figure 1.3. 2D schematic of the ref. configuration of a closed-cell foam RVE.

configuration, respectively. The exterior boundary is $\partial\Omega_0^E$, and the inner boundary (where the solid is in contact with the fluid) is $\partial\Omega_0^N$, see Figure 1.3 for a schematic. Let \mathcal{V}_u and \mathcal{V}_p be suitable spaces for the fields \mathbf{u} and p , respectively; and let \mathcal{V}_u^0 and \mathcal{V}_p^0 be the suitable spaces for the admissible perturbation fields $\delta\mathbf{u}$ and δp . In absence of body forces, the total potential energy is

$$\Pi_{\text{tot}}(\mathbf{u}, p) := \int_{\Omega_0^S} [\psi_{\text{iso}}(\mathbf{F}) - p(J - 1)] dV - p_0 \int_{\Omega_0^F} J dV, \quad (1.22)$$

with p_0 the pore pressure of the fluid. Then, the stationary conditions are

$$\begin{aligned} D_{\delta\mathbf{u}}\Pi_{\text{tot}}(\mathbf{u}, p) &= - \int_{\Omega_0^S} (\nabla_0 \cdot \bar{\mathbf{P}}) \cdot \delta\mathbf{u} dV + \int_{\partial\Omega_0^E} \bar{\mathbf{P}}\mathbf{N} \cdot \delta\mathbf{u} dS \\ &\quad + \int_{\partial\Omega_0^N} (\bar{\mathbf{P}}\mathbf{N} + p_0 J \mathbf{F}^{-T} \mathbf{N}) \cdot \delta\mathbf{u} dS = 0 \quad \forall \delta\mathbf{u} \in \mathcal{V}_u^0, \end{aligned} \quad (1.23)$$

and

$$D_{\delta p}\Pi_{\text{tot}}(\mathbf{u}, p) = \int_{\Omega_0^S} \delta p(J - 1) dV = 0 \quad \forall \delta p \in \mathcal{V}_p^0, \quad (1.24)$$

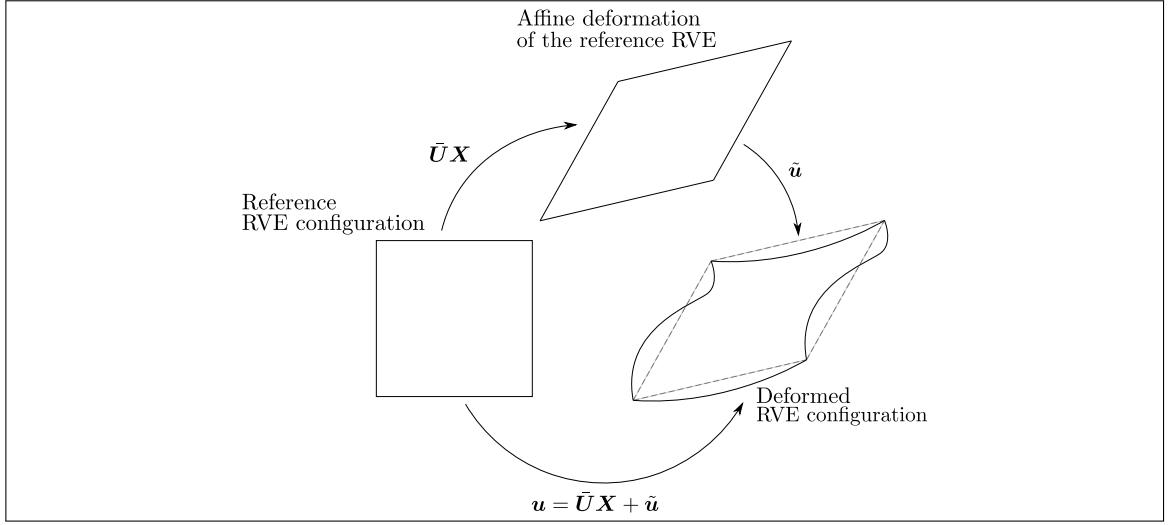


Figure 1.4. The displacement in the RVE can be decomposed into an affine term, characterized by a constant deformation gradient tensor, plus a fluctuation field. Different kinematical constraints on the fluctuation field can be imposed; in this figure, periodic boundary conditions are illustrated. Adapted from De Souza Neto and Feijóo (2006).

Then, the strong form of the problem is: Given p_0 , find $\mathbf{u} \in \mathcal{V}_u$ and $p \in \mathcal{V}_p$, such that

$$\left. \begin{aligned} \nabla_0 \cdot \bar{\mathbf{P}}(\mathbf{F}, p) &= \mathbf{0} && \text{in } \Omega_0^S, \\ \bar{\mathbf{P}}(\mathbf{F}, p)\mathbf{N} &= -p_0 J \mathbf{F}^{-T} \mathbf{N} && \text{on } \partial\Omega_0^N, \\ J(\mathbf{F}) &= 1 && \text{in } \Omega_0^S, \\ \mathbf{F} &= \mathbf{I} + \nabla_0 \mathbf{u} && \text{in } \Omega_0^S. \end{aligned} \right\} \quad (1.25)$$

This formulation has to be completed with the choice of boundary conditions for the exterior of the RVE, $\partial\Omega_0^E$. As in the pressure-driven case the stress and strain fields are a reaction to the applied pressure, and hence there are no values given for the displacement or pressure on the exterior boundary, further assumptions are required. In this work, instead of imposing states like uniaxial compression or simple shear, we will enforce kinematical constraints on the displacement field. These constraints are based on the ones classically used in multiscale simulations, which will be detailed in the next section.

1.3.5. Decomposition of the displacement and kinematical constraints

So far, the problem was stated in terms of the displacement field \mathbf{u} ; however, a common approach in mechanical models based on homogenization theory, is to express \mathbf{u} as a sum of an affine component and a fluctuation field

$$\mathbf{u}(\mathbf{X}) = \bar{\mathbf{U}}\mathbf{X} + \tilde{\mathbf{u}}(\mathbf{X}), \quad (1.26)$$

where the tensor $\bar{\mathbf{U}}$ will be referred as the macroscopic strain, and $\tilde{\mathbf{u}}(\mathbf{X})$ is the fluctuation field; this decomposition is illustrated in Figure 1.4. The problem has to be completed with a constraint on the fluctuation term, among the most usual are (Perić et al., 2011; Saeb et al., 2016):

- (i) Taylor model: the fluctuation field vanishes

$$\tilde{\mathbf{u}}(\mathbf{X}) = \mathbf{0} \quad \forall \mathbf{X} \text{ in } \Omega_0, \quad (1.27)$$

which leads to a constant deformation in Ω_0 , being the deformation gradient tensor $\mathbf{F} = \mathbf{I} + \bar{\mathbf{U}}$. This is also known as the Voigt bound.

- (ii) Kinematic uniform boundary condition (KUBC, or linear displacement boundary condition): the fluctuation field vanishes only on the boundary of the RVE,

$$\tilde{\mathbf{u}}(\mathbf{X}) = \mathbf{0} \quad \forall \mathbf{X} \text{ on } \partial\Omega_0^E. \quad (1.28)$$

- (iii) Periodic displacement boundary condition (PBC): used to represent that the RVE is surrounded by identical cells, forming a periodic material. Here, it is assumed that the boundary $\partial\Omega_0^E$ is periodic, so there exist pairs $\{\mathbf{X}^+, \mathbf{X}^-\}$ that relate the coordinates of two periodic faces, as illustrated in Figure 1.5. A geometrical interpretation of this is that the surface where \mathbf{X}^+ is defined, is equal to the surface of \mathbf{X}^- , but translated. Then, the fluctuation field is enforced to be periodic

$$\tilde{\mathbf{u}}(\mathbf{X}^+) = \tilde{\mathbf{u}}(\mathbf{X}^-) \quad \forall \text{ pairs } \{\mathbf{X}^+, \mathbf{X}^-\}, \quad (1.29)$$

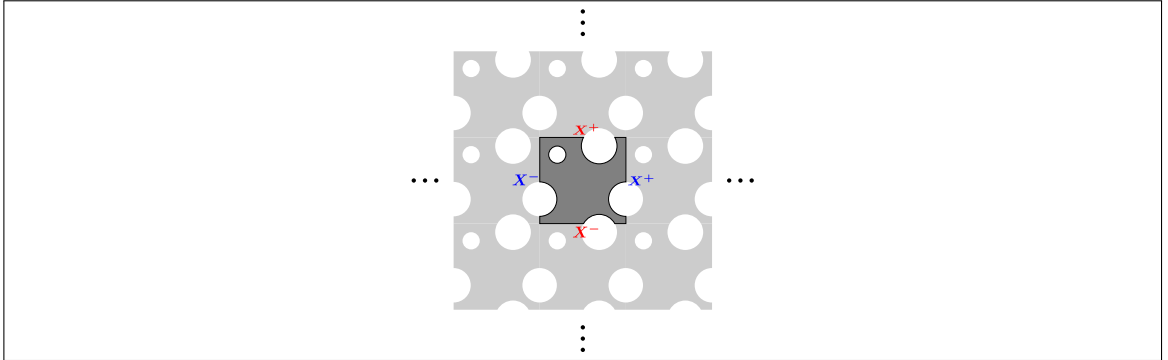


Figure 1.5. 2D schematic of a periodic RVE. In the external boundary there are pairs $\{\mathbf{X}^+, \mathbf{X}^-\}$ that relate the coordinates of two periodic faces. Here, in blue a pair that relates two coordinates of the lateral faces, while in red the upper and lower ones.

which implies that the tractions on the periodic boundaries be anti-periodic

$$(\mathbf{P}\mathbf{N})^+ = -(\mathbf{P}\mathbf{N})^- \quad \forall \text{ pairs } \{\mathbf{X}^+, \mathbf{X}^-\}, \quad (1.30)$$

where $(\mathbf{P}\mathbf{N})^\pm = \mathbf{P}(\mathbf{F}(\mathbf{X}^\pm))\mathbf{N}(\mathbf{X}^\pm)$.

- (iv) Uniform traction boundary conditions (or stress uniform boundary conditions, SUBC): the first Piola-Kirchhoff stress tensor is constant in the boundary, producing a uniform traction \mathbf{T} ,

$$\mathbf{T} := \mathbf{P}\mathbf{N} = \mathbf{P}^c\mathbf{N} \quad \forall \mathbf{X} \quad \text{on } \partial\Omega_0^E, \quad (1.31)$$

where \mathbf{P}^c is a constant tensor.

- (v) Reuss model: the stress is constant in Ω_0 ,

$$\mathbf{P} = \mathbf{P}^c \quad \text{in } \Omega_0, \quad (1.32)$$

where \mathbf{P}^c is a constant tensor.

For a given macroscopic strain, the first four constraints can be also understood as selecting a proper space $\mathcal{V}_{\tilde{\mathbf{u}}}$ for the fluctuation field, such that $\tilde{\mathbf{u}} \in \mathcal{V}_{\tilde{\mathbf{u}}}$. Then, each constraint

is identified with a definition of this space, which can be related as

$$\mathcal{V}_{\tilde{u}}^{\text{Taylor}} \subset \mathcal{V}_{\tilde{u}}^{\text{kubc}} \subset \mathcal{V}_{\tilde{u}}^{\text{pbc}} \subset \mathcal{V}_{\tilde{u}}^{\text{subc}}, \quad (1.33)$$

where the superscript indicates the respective constraint (De Souza Neto & Feijóo, 2006). This means the Taylor model gives the stiffest solution to the micromechanical problem, followed in order of decreasing stiffness by the kinematic uniform, the periodic displacement and the uniform traction models. These relations agree with the well-known influence of the constraints on the effective response of composites (Carniel et al., 2019; Kanit et al., 2003; Terada et al., 2000); however, their implications in the micromechanical response of pressure-driven OCFs is still understudied.

1.4. Thesis Structure

This thesis is divided into four chapters; the first one presented an introduction to the micromechanical study of porous materials and detailed the basis for the variational framework that will be adopted. The second chapter consists of the article in which this thesis is based: “Pressure-driven micro-poro-mechanics: A variational framework for modeling the response of porous materials”; this paper presents a variational framework for the micromechanical analysis of pressure-driven porous materials and then applies it in numerical simulations of the lung parenchyma. Three appendices are included, which extend the scope of the article. The third chapter presents the conclusions of this thesis, and the fourth one the future work, detailing possible improvements and applications of the present work.

2. PRESSURE-DRIVEN MICRO-PORO-MECHANICS: A VARIATIONAL FRAMEWORK FOR MODELING THE RESPONSE OF POROUS MATERIALS¹

2.1. Introduction

Porous materials are ubiquitous in nature and engineering applications, and take shape as saturated rocks, polymer foams, plant cells and biological tissues among others. One kind of porous materials are open-cell foams (OCFs), which are defined as materials composed of a matrix with interconnected cavities (Ma et al., 2011). This structural arrangement strongly influences the mechanical response of OCFs, which is dominated by mechanisms such as bending of struts, buckling of cell walls, the formation of yield joints or folds, and fracture of cell struts and cell walls (Altenbach & Öchsner, 2010). Due to its permeability, cavities in OCFs can be subject to pressure exerted by a fluid or a gas, which can drive the mechanical response of the material. Examples of pressurized materials are the foams used to thermally insulate the Space Shuttle external tank (Bednarczyk et al., 2008), where thermoelastic and thermoinelastic effects are also present; the lung parenchyma, where alveoli are subject to internal air pressure (Koshiyama et al., 2019; Rausch et al., 2011; Sarabia-Vallejos et al., 2019); the brain tissue permeated by blood and cerebrospinal fluid (Guo et al., 2020); and porous elastomers, where the presence of pressurized cavities has proven to affect the overall response, producing, for instance, the shrinkage of elastomeric foams after demolding (Fen-Chong et al., 1999; Idiart & Lopez-Pamies, 2012).

The constitutive response of porous materials has been approached in engineering by means of traditional poromechanics theory, focused on a macroscopic approach (Biot, 1941; Chapelle & Moireau, 2014; Coussy, 2004), and more recently including micromechanical effects (Dormieux et al., 2002). Computational micromechanical models have been developed for many types of materials, but only few for OCFs, especially in the finite

¹This chapter corresponds to the submitted article “Pressure-driven micro-poro-mechanics: A variational framework for modeling the response of porous materials”, by Felipe Álvarez, Daniel Hurtado and Martin Genet.

deformation setting. To this end, a representative volume element (RVE) of the underlying microstructure of the material must be constructed, based on which a microstructural problem is solved to obtain the stress and strain distributions in the RVE. Then, the effective behavior can be obtained by averaging the stress and strain fields arising in the RVE (Hashin, 1983; Hill, 1963; Suquet, 1987). In order to model OCFs, RVEs can be constructed from micro-computed-tomography (micro-CT) images of the microstructure, conferring the RVE a highly realistic geometry of the material, that allows to study the material response at the micro level. This approach has been used, for example, in models of polyurethane foams (Youssef et al., 2005), metallic foams (Kantzos et al., 2018) and pulmonary alveoli (Roth et al., 2017), giving information about local deformation mechanisms, such as regions of stress concentrations.

In addition to the creation of the RVE, micromechanical models of porous materials necessitate the definition of suitable boundary conditions (BCs), and internal loads. When experimental data is available, the boundary conditions in the RVE can be obtained from sets of 3D images using Digital Volume Correlation, or with methods to relate the conditions of the whole specimen to the conditions in the RVE, based on macroscopic homogenized properties (Shakoor et al., 2017). However, in the lack of experimental data, and to avoid obtaining homogenized quantities, further assumptions have to be made to determine the boundary conditions of the RVE. One option is to use the classical boundary conditions adopted in homogenization and multi-scale simulations (Fish, 2013; Hill, 1963; Hollister & Kikuchi, 1992; Saeb et al., 2016; Suquet, 1987), where the displacement field is decomposed into an affine component and a fluctuation field, and according to the boundary condition selected, different constraints are applied in the fluctuation term. Five conditions are commonly adopted: i) Voigt bound model, where the displacement field is assumed to be affine everywhere inside the RVE and the fluctuation field vanishes, ii) kinematic uniform boundary condition (KUBC), where the fluctuation vanishes at the boundary but is otherwise unknown in the domain of the RVE, iii) periodic displacement boundary condition (PBC), where the fluctuation field is periodic at the boundary, iv) uniform traction boundary condition (SUBC), which can be interpreted as an integral

constraint on the fluctuation field, and v) Reuss model, where the stress field is homogeneous everywhere inside the RVE. While the effect of these constraints on the coarse-scale response of composites is known (Carniel et al., 2019; Kanit et al., 2003; Terada et al., 2000), their implications in the distribution of stresses at the microscale in foams driven by pore pressure is still understudied.

Micromechanical analysis of foams have been focused on the cases where the macroscopic strain, or the macroscopic stress, are imposed (De Souza Neto & Feijóo, 2006; Perić et al., 2011). However, in porous materials the pore pressure can drive the deformation, with the macroscopic strain and stress being a response of the system. For example, this case is present when the loading process of pressurized foams is decomposed into two steps: first, an initial configuration is obtained, where the deformation in the RVE is produced only by the pore pressure, and then, the final deformed configuration is obtained by applying the external loads. The pressure-driven case has been predominantly approached by means of numerical simulations, with less developments from an analytical perspective. To implement it, computational simulations have been conducted imposing restrictions between the degrees of freedom of the boundaries on the discretized system. Ma et al. (2011) developed a micromechanical model for fluid-filled closed-cell composites with pore pressure and external loads, where first they obtained the response with pore pressure only, imposing periodic boundary conditions by coupling constraint equations and obtaining the macroscopic strain as a result of the simulation. In another example, Ju et al. (2008) modeled balloon-expandable stents as cylindrical structures with longitudinal and circumferential periodicity, subject to internal pressure. Similar to the previous case, the elongation in the z -direction is unknown before finite element computations, and it is excluded from the displacement constraint equations by the use of multiple-point constraints. Despite the existence of these numerical constraints, which allow the pressure-driven model to be numerically solved, a general analysis of the boundary conditions for the continuous mechanical problem of pressurized foams remains an open avenue of research.

In this paper, we present a variational framework for modeling the pressure-driven response of RVEs of foam materials, in the setting of finite kinematics. The theoretical analysis of the problem is completed with the choice of boundary conditions, which are expressed as kinematical constraints in the fluctuation term of the displacement, among which three options are compared: KUBC, PBC and SUBC. After the variational framework is developed, the proposed model is used to study the micromechanical response in the context of lung parenchyma simulations. Moreover, the numerical simulations will help to understand the potential differences when the tissue microstructure is replaced by an idealized representation. We conclude by analyzing the implications of the different boundary conditions (KUBC, PBC and SUBC), and loadings (pressure, deformation), in terms of the stress distributions obtained.

2.2. Micromechanical Model: Variational Framework

In the following, we develop a variational framework for finite-strain micromechanical analysis of pressure-driven foam materials, i.e., porous materials for which the pore pressure is known and the macroscopic strain is an unknown of the problem. Let Ω_0^S and Ω^S be the solid domain in the reference and current configurations, respectively, and let Ω_0^F and Ω^F represent the fluid domain in the reference and current configurations, respectively. Then, the RVE domain in the reference configuration is $\Omega_0 = \Omega_0^S \cup \Omega_0^F$. Similarly, the current configuration is constructed as $\Omega = \Omega^S \cup \Omega^F$. Let $\partial\Omega_0^E$ and $\partial\Omega_0^N$ be the outer and inner boundaries, respectively, in the reference configuration, and $\partial\Omega^E$ and $\partial\Omega^N$ be their counterparts in the current configuration, see Figure 2.1a for a graphical representation. Note that, in general, $\partial\Omega_0^E$ is only a subset of the total boundary of the RVE, because in OCFs the pores intersect the RVE border. The deformation mapping $\varphi : \Omega_0 \rightarrow \Omega$ maps a point \mathbf{X} in the reference configuration into its corresponding position in the current configuration, denoted by \mathbf{x} , such that $\varphi(\mathbf{X}) = \mathbf{x}$. Further, we define the deformation gradient tensor field \mathbf{F} as

$$\mathbf{F} := \frac{\partial\varphi}{\partial\mathbf{X}}(\mathbf{X}). \quad (2.1)$$

Without loss of generality, we decompose the displacement field \mathbf{u} as a sum of an affine transformation and a fluctuation field

$$\mathbf{u}(\mathbf{X}) = \bar{\mathbf{U}} \hat{\mathbf{X}} + \tilde{\mathbf{u}}, \quad (2.2)$$

where $\bar{\mathbf{U}} \in \mathcal{V}_{\bar{\mathbf{U}}} = \text{Sym}_n$ (space of $(n \times n)$ symmetric matrices), $\tilde{\mathbf{u}} : \Omega_0 \rightarrow \mathbb{R}^3$ is the fluctuation field, and $\hat{\mathbf{X}} := \mathbf{X} - \mathbf{X}_0$, with \mathbf{X}_0 a point in the reference configuration. The case where the macroscopic strain $\bar{\mathbf{U}}$ is given has been widely studied, with a remarkable theoretical approach adopted by De Souza Neto and Feijóo (2006) and Perić et al. (2011), where they develop the variational formulation of the problem and analyze different kinematical constraints on the fluctuation term, needed to make the problem well-posed; in contrast, note that here both $\bar{\mathbf{U}}$ and $\tilde{\mathbf{u}}$ are unknowns of the problem. As $\bar{\mathbf{U}}$ is a variable of the problem, the affine transformation can capture a scaling, shear and/or rotation of the RVE; however, we assume the pore pressure does not produce rotations, which is the reason why $\bar{\mathbf{U}}$ is symmetric. The explanation of this lies in the polar decomposition theorem, that states the deformation gradient can be decomposed uniquely as the product of two tensors: an orthogonal one, that corresponds to a rotation, and a symmetric one, that describes the deformation. Then, the purpose of enforcing $\bar{\mathbf{U}}$ to be symmetric is to capture only the component of deformation. For the fluctuation field, as done in Perić et al. (2011) and De Souza Neto and Feijóo (2006), we study the implications of different kinematical constraints, which corresponds to define suitable spaces $\mathcal{V}_{\tilde{\mathbf{u}}}$ such that $\tilde{\mathbf{u}} \in \mathcal{V}_{\tilde{\mathbf{u}}}$.

We model the mechanical behavior of the RVE using a variational approach, where we assume that the solid phase of the microstructure follows an incompressible hyperelastic behavior that is driven by the pore pressure. Within this framework, we define the internal energy of deformation by

$$\Pi_{\text{int}}(\bar{\mathbf{U}}, \tilde{\mathbf{u}}, p) = \int_{\Omega_0^s} \psi(\mathbf{F}, p) dV, \quad (2.3)$$

with

$$\psi(\mathbf{F}, p) := \psi_{\text{iso}}(\mathbf{F}) - p(J - 1), \quad \mathbf{F} = \mathbf{I} + \bar{\mathbf{U}} + \nabla_0 \tilde{\mathbf{u}}, \quad (2.4)$$

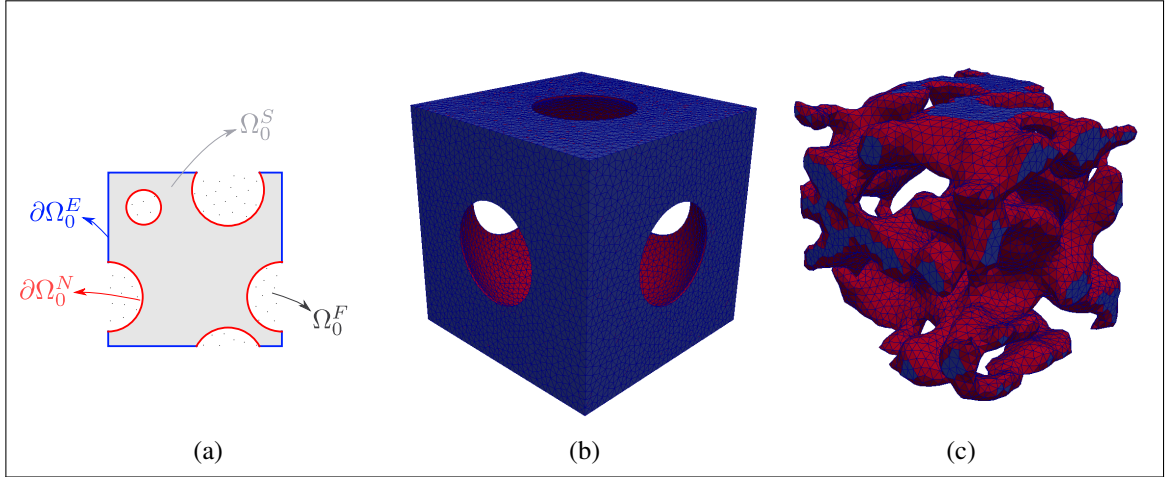


Figure 2.1. (a) 2D schematic of the ref. configuration of a periodic foam-like material RVE. In gray, the solid domain, while in blue and red, its bounding and inner boundaries, respectively. The colors in (b) and (c) are consistent with this definition. (b) Mesh of the spherical alveolar model, representing a spherical alveolus in the parenchyma. (c) Mesh of the image-based alveolar model, obtained by micro-CT images of rat lung parenchyma. For further details, refer to section 2.3.

where p represents a Lagrange multiplier field needed to enforce the incompressibility condition in the formulation, $\psi(\mathbf{F}, p)$ is the strain energy density function of the incompressible solid, $\psi_{\text{iso}}(\mathbf{F})$ characterizes its isochoric response and $J := \det \mathbf{F}$. The external potential energy is defined as

$$\Pi_{\text{ext}}(\bar{\mathbf{U}}, \tilde{\mathbf{u}}) = -p_0 V^F, \quad (2.5)$$

where p_0 is the pore pressure exerted by the fluid, and $V^F := |\Omega^F|$ the current fluid volume. We note that, as the traction induced by the pore pressure on the inner boundary of the solid depends on the current configuration, and therefore on the deformation mapping, it cannot be always included in the potential energy as it may not derive from a potential density. In our case, we can include it because the fluid domain is enclosed by a surface (Bonet & Wood, 1997), composed by the inner boundary of the solid $\partial\Omega_0^N$ and the external boundary of the pores. As in the present work we are not interested in the fluid response, we impose the displacement to be zero ($\mathbf{u} = \mathbf{0}$) in the external boundary of the pores, so

in the stationarity conditions the only relevant term associated to p_0 is

$$\begin{aligned} D_{\delta \mathbf{u}} \Pi_{\text{ext}}(\mathbf{u}) &= \int_{\partial \Omega_0^N} p_0 J \mathbf{F}^{-T} \mathbf{N} \cdot \delta \mathbf{u} \, dS \\ &= \int_{\partial \Omega_0^N} p_0 J \mathbf{F}^{-T} \mathbf{N} \cdot (\delta \bar{\mathbf{U}} \hat{\mathbf{X}} + \delta \tilde{\mathbf{u}}) \, dS, \end{aligned} \quad (2.6)$$

which is expressed as an integral on the solid inner boundary $\partial \Omega_0^N$.

Based on the definitions above, we express the total potential energy as

$$\Pi_{\text{tot}} := \Pi_{\text{int}} + \Pi_{\text{ext}}. \quad (2.7)$$

Then, from the Principle of stationary potential energy, we find the variational equations needed for the RVE equilibrium, starting with the stationary condition of $\tilde{\mathbf{u}}$

$$\begin{aligned} D_{\delta \tilde{\mathbf{u}}} \Pi_{\text{tot}}(\bar{\mathbf{U}}, \tilde{\mathbf{u}}, p) &= \int_{\partial \Omega_0^E} \bar{\mathbf{P}} \mathbf{N} \cdot \delta \tilde{\mathbf{u}} \, dS - \int_{\Omega_0^S} (\nabla_0 \cdot \bar{\mathbf{P}}) \cdot \delta \tilde{\mathbf{u}} \, dV \\ &+ \int_{\partial \Omega_0^N} (\bar{\mathbf{P}} \mathbf{N} + p_0 J \mathbf{F}^{-T} \mathbf{N}) \cdot \delta \tilde{\mathbf{u}} \, dS = 0 \quad \forall \delta \tilde{\mathbf{u}} \in \mathcal{V}_{\tilde{\mathbf{u}}}^0, \end{aligned} \quad (2.8)$$

where $\mathcal{V}_{\tilde{\mathbf{u}}}^0$ is a suitable space for the admissible perturbation field $\delta \tilde{\mathbf{u}}$, and $\bar{\mathbf{P}}$ is the first Piola-Kirchhoff stress tensor

$$\bar{\mathbf{P}}(\mathbf{F}, p) := \frac{\partial \psi}{\partial \mathbf{F}}(\mathbf{F}, p) = \frac{\partial \psi_{\text{iso}}}{\partial \mathbf{F}}(\mathbf{F}) - p J \mathbf{F}^{-T}. \quad (2.9)$$

Then, from Equation (2.8) we can deduce

$$\nabla_0 \cdot \bar{\mathbf{P}} = \mathbf{0} \quad \text{in } \Omega_0^S, \quad (2.10)$$

$$\bar{\mathbf{P}} \mathbf{N} = -p_0 J \mathbf{F}^{-T} \mathbf{N} \quad \text{on } \partial \Omega_0^N, \quad (2.11)$$

the missing relation for $\partial \Omega_0^E$ depends on the kinematical constraint for $\tilde{\mathbf{u}}$, and it will be analyzed in the next section.

The stationarity with respect to \bar{U} yields

$$D_{\delta\bar{U}}\Pi_{\text{tot}}(\bar{U}, \tilde{\mathbf{u}}, p) = \int_{\Omega_0^S} \bar{\mathbf{P}} : \nabla_0(\delta\bar{U} \hat{\mathbf{X}}) dV + \int_{\partial\Omega_0^N} p_0 J \mathbf{F}^{-T} \mathbf{N} \cdot \delta\bar{U} \hat{\mathbf{X}} dS = 0 \quad \forall \delta\bar{U} \in \mathcal{V}_{\bar{U}}, \quad (2.12)$$

however, noting that \bar{U} does not depend on \mathbf{X} , the first term can be expressed as

$$\int_{\Omega_0^S} \bar{\mathbf{P}} : \nabla_0(\delta\bar{U} \hat{\mathbf{X}}) dV = \int_{\Omega_0^S} \bar{\mathbf{P}} : \delta\bar{U} dV = \int_{\Omega_0^S} \bar{\mathbf{P}} dV : \delta\bar{U}, \quad (2.13)$$

then,

$$D_{\delta\bar{U}}\Pi_{\text{tot}}(\bar{U}, \tilde{\mathbf{u}}, p) = \left[\int_{\Omega_0^S} \bar{\mathbf{P}} dV + \int_{\partial\Omega_0^N} p_0 J \mathbf{F}^{-T} \mathbf{N} \otimes \hat{\mathbf{X}} dS \right] : \delta\bar{U} = 0 \quad \forall \delta\bar{U} \in \mathcal{V}_{\bar{U}}. \quad (2.14)$$

The macroscopic first Piola-Kirchhoff stress tensor in the solid domain is defined as

$$\langle \bar{\mathbf{P}} \rangle := \frac{1}{|\Omega_0^S|} \int_{\Omega_0^S} \bar{\mathbf{P}} dV, \quad (2.15)$$

and replacing it in Equation (2.14)

$$\left[|\Omega_0^S| \langle \bar{\mathbf{P}} \rangle + \int_{\partial\Omega_0^N} p_0 J \mathbf{F}^{-T} \mathbf{N} \otimes \hat{\mathbf{X}} dS \right] : \delta\bar{U} = 0 \quad \forall \delta\bar{U} \in \mathcal{V}_{\bar{U}}, \quad (2.16)$$

which, due to the symmetry of \bar{U} , implies the following equation

$$|\Omega_0^S| \left(\langle \bar{\mathbf{P}} \rangle + \langle \bar{\mathbf{P}} \rangle^T \right) = - \int_{\partial\Omega_0^N} (p_0 J \mathbf{F}^{-T} \mathbf{N} \otimes \hat{\mathbf{X}}) + (\hat{\mathbf{X}} \otimes p_0 J \mathbf{F}^{-T} \mathbf{N}) dS, \quad (2.17)$$

that can be interpreted as a relation between the macroscopic first Piola-Kirchhoff stress tensor and the pressure applied on the inner boundary. However, as the deformation gradient tensor depends on \bar{U} and $\tilde{\mathbf{u}}$, this relation is coupled with the rest of the equations, and the macroscopic stress cannot be obtained *a priori*.

For the Lagrange multiplier p , the stationarity corresponds to

$$D_{\delta p}\Pi_{\text{tot}}(\bar{U}, \tilde{\mathbf{u}}, p) = \int_{\Omega_0^S} \delta p (J - 1) dV = 0 \quad \forall \delta p \in \mathcal{V}_p^0, \quad (2.18)$$

where \mathcal{V}_p^0 is a suitable space for the admissible perturbation field δp . This Equation implies the incompressibility of the solid, that in terms of $J(\mathbf{F})$ is

$$J(\mathbf{F}) = 1 \quad \text{in } \Omega_0^S. \quad (2.19)$$

2.2.1. Kinematical constraints

To complete the problem, a suitable space for the displacement fluctuation must be selected. We will discuss three options commonly adopted:

- (i) **Kinematic uniform boundary condition (KUBC):** The boundary displacement fluctuation vanishes

$$\mathcal{V}_{\tilde{\mathbf{u}}} = \mathcal{V}_{\tilde{\mathbf{u}}}^{\text{kubc}} := \{\tilde{\mathbf{u}} \in H^1(\Omega_0^S) \mid \tilde{\mathbf{u}}(\mathbf{X}) = \mathbf{0} \quad \forall \mathbf{X} \text{ on } \partial\Omega_0^E\}, \quad (2.20)$$

$$\mathcal{V}_p = \mathcal{V}_p^{\text{kubc}} := L^2(\Omega_0^S). \quad (2.21)$$

- (ii) **Periodic displacement boundary condition (PBC):** Used to describe materials with periodic microstructure, here it is assumed that the boundary $\partial\Omega_0^E$ is periodic, so there exists pairs $\{\mathbf{X}^+, \mathbf{X}^-\}$ that relate the coordinates of two periodic faces. In this case

$$\mathcal{V}_{\tilde{\mathbf{u}}} = \mathcal{V}_{\tilde{\mathbf{u}}}^{\text{pbc}} := \{\tilde{\mathbf{u}} \in H^1(\Omega_0^S) \mid \tilde{\mathbf{u}}(\mathbf{X}^+) = \tilde{\mathbf{u}}(\mathbf{X}^-) \quad \forall \text{ pairs } \{\mathbf{X}^+, \mathbf{X}^-\}\}, \quad (2.22)$$

$$\mathcal{V}_p = \mathcal{V}_p^{\text{pbc}} := \{p \in L^2(\Omega_0^S) \mid p(\mathbf{X}^+) = p(\mathbf{X}^-) \quad \forall \text{ pairs } \{\mathbf{X}^+, \mathbf{X}^-\}\}. \quad (2.23)$$

As in $\partial\Omega_0^E$ the fluctuation $\tilde{\mathbf{u}}$ is periodic, from the first term in Equation (2.8)

$$\int_{\partial\Omega_0^E} \bar{\mathbf{P}}\mathbf{N} \cdot \delta\tilde{\mathbf{u}} \, dS = 0 \quad \forall \delta\tilde{\mathbf{u}} \in \mathcal{V}_{\tilde{\mathbf{u}}}^0, \quad (2.24)$$

and we see the periodicity in the fluctuation term implies the anti-periodicity of the traction $\bar{\mathbf{P}}\mathbf{N}$ on the external boundary

$$(\bar{\mathbf{P}}\mathbf{N})^+ = -(\bar{\mathbf{P}}\mathbf{N})^- \quad \text{on } \partial\Omega_0^E, \quad (2.25)$$

where $(\bar{\mathbf{P}}\mathbf{N})^+$ and $(\bar{\mathbf{P}}\mathbf{N})^-$ correspond to the traction in the periodic pairs \mathbf{X}^+ and \mathbf{X}^- , respectively.

- (iii) Uniform traction boundary condition (also known as stress uniform boundary conditions, SUBC): the traction is uniform in the boundary, with the first Piola-Kirchhoff stress tensor constant. This condition can be enforced with a Lagrange multiplier (Javili et al., 2017), adding a term in the external potential energy

$$\Pi_{\text{ext}}(\bar{\mathbf{U}}, \tilde{\mathbf{u}}, \boldsymbol{\lambda}) = p_0 V^F + \boldsymbol{\lambda} : \int_{\partial\Omega_0^E} \tilde{\mathbf{u}} \otimes \mathbf{N} dS, \quad (2.26)$$

where $\boldsymbol{\lambda} \in M_3$ is the Lagrange multiplier, with M_n the space of all $(n \times n)$ matrices. Note that $\boldsymbol{\lambda}$ is outside the integral because it is a constant tensor, that does not depend on \mathbf{X} , however, this term could also be written as $\int_{\partial\Omega_0^E} \boldsymbol{\lambda} \mathbf{N} \cdot \tilde{\mathbf{u}} dS$. Then, the stationary condition of $\tilde{\mathbf{u}}$ yields

$$\begin{aligned} D_{\delta\tilde{\mathbf{u}}}\Pi_{\text{tot}}(\bar{\mathbf{U}}, \tilde{\mathbf{u}}, p, \boldsymbol{\lambda}) &= \int_{\partial\Omega_0^E} (\bar{\mathbf{P}}\mathbf{N} - \boldsymbol{\lambda}\mathbf{N}) \cdot \delta\tilde{\mathbf{u}} dS - \int_{\Omega_0^S} (\nabla_0 \cdot \bar{\mathbf{P}}) \cdot \delta\tilde{\mathbf{u}} dV \\ &+ \int_{\partial\Omega_0^N} (\bar{\mathbf{P}}\mathbf{N} + p_0 J \mathbf{F}^{-T} \mathbf{N}) \cdot \delta\tilde{\mathbf{u}} dS = 0 \quad \forall \delta\tilde{\mathbf{u}} \in \mathcal{V}_{\tilde{\mathbf{u}}}^0, \end{aligned} \quad (2.27)$$

from which we obtain Equations (2.10), (2.11) and the uniform traction condition

$$\bar{\mathbf{P}}\mathbf{N} = \boldsymbol{\lambda}\mathbf{N} \quad \text{on } \partial\Omega_0^E. \quad (2.28)$$

The stationarity with respect to $\bar{\mathbf{U}}$ is equal to the developed in the previous section, and with respect to $\boldsymbol{\lambda}$ is

$$D_{\delta\boldsymbol{\lambda}}\Pi_{\text{tot}}(\tilde{\mathbf{u}}, \boldsymbol{\lambda}) = \delta\boldsymbol{\lambda} : \int_{\partial\Omega_0^E} \tilde{\mathbf{u}} \otimes \mathbf{N} dS = 0 \quad \forall \delta\boldsymbol{\lambda} \in M_3, \quad (2.29)$$

which implies

$$\int_{\partial\Omega_0^E} \tilde{\mathbf{u}} \otimes \mathbf{N} dS = \mathbf{0}. \quad (2.30)$$

This suggests the definition of the space $\mathcal{V}_{\tilde{\mathbf{u}}}^{\text{subc}}$ as

$$\mathcal{V}_{\tilde{\mathbf{u}}}^{\text{subc}} := \{ \tilde{\mathbf{u}} \in H^1(\Omega_0^S) \mid \int_{\partial\Omega_0^E} \tilde{\mathbf{u}} \otimes \mathbf{N} dS = \mathbf{0} \}. \quad (2.31)$$

Then, the spaces $\mathcal{V}_{\tilde{u}}^{\text{kubc}}$, $\mathcal{V}_{\tilde{u}}^{\text{pbc}}$ and $\mathcal{V}_{\tilde{u}}^{\text{subc}}$ can be related as

$$\mathcal{V}_{\tilde{u}}^{\text{kubc}} \subset \mathcal{V}_{\tilde{u}}^{\text{pbc}} \subset \mathcal{V}_{\tilde{u}}^{\text{subc}}. \quad (2.32)$$

The first relation is direct, due to the vanishing of the boundary fluctuations in the KUBC case. For the periodic case, the condition $\int_{\partial\Omega_0^E} \tilde{\mathbf{u}} \otimes \mathbf{N} \, dS = \mathbf{0}$ is accomplished due to the periodicity of $\tilde{\mathbf{u}}$ and the anti-periodicity of \mathbf{N} .

For p , in this case

$$\mathcal{V}_p = \mathcal{V}_p^{\text{subc}} = L^2(\Omega_0^S). \quad (2.33)$$

Previously, based on the polar decomposition theorem, we enforced $\bar{\mathbf{U}}$ to be symmetric. For the PBC and SUBC, we can additionally show that if the external forces (due to the pore pressure, or body force if present) produce an angular momentum different from zero, then $\bar{\mathbf{U}}$ must be symmetric, as detailed in Appendix A.

Finally, we can express the strong form of the problem as: Given p_0 , find $\bar{\mathbf{U}} \in \mathcal{V}_{\bar{\mathbf{U}}}$, $\tilde{\mathbf{u}} \in \mathcal{V}_{\tilde{u}}$ and $p \in \mathcal{V}_p$, such that

$$\left. \begin{aligned} \nabla_0 \cdot \bar{\mathbf{P}}(\mathbf{F}, p) &= \mathbf{0} && \text{in } \Omega_0^S, \\ \bar{\mathbf{P}}(\mathbf{F}, p)\mathbf{N} &= -p_0 J \mathbf{F}^{-T} \mathbf{N} && \text{on } \partial\Omega_0^N, \\ J(\mathbf{F}) &= 1 && \text{in } \Omega_0^S, \\ \mathbf{F} &= \mathbf{I} + \bar{\mathbf{U}} + \nabla_0 \tilde{\mathbf{u}} && \text{in } \Omega_0^S, \\ |\Omega_0^S| \left(\langle \bar{\mathbf{P}} \rangle + \langle \bar{\mathbf{P}} \rangle^T \right) &= - \int_{\partial\Omega_0^N} (p_0 J \mathbf{F}^{-T} \mathbf{N} \otimes \hat{\mathbf{X}}) && \\ &\quad + (\hat{\mathbf{X}} \otimes p_0 J \mathbf{F}^{-T} \mathbf{N}) \, dS. && \end{aligned} \right\} (2.34)$$

Plus,

$$(\bar{\mathbf{P}}\mathbf{N})^+ = -(\bar{\mathbf{P}}\mathbf{N})^- \quad \text{on } \partial\Omega_0^E \quad \text{for PBC,}$$

$$\bar{\mathbf{P}}(\mathbf{F}, p)\mathbf{N} = \boldsymbol{\lambda} \mathbf{N} \quad \text{on } \partial\Omega_0^E \quad \text{for SUBC, with } \boldsymbol{\lambda} \in \mathbb{M}_3 \text{ a variable of the problem.}$$

The case including body force is analogous, and is detailed in Appendix B.

2.3. Numerical Examples

The proposed variational framework can be applied to the study of different kinds of pressurized foams. In this section, we will focus on the behavior of the lung tissue, a pressurized biological foam, through two examples: first, a spherical alveolar model, representing a single spherical alveolus inside a box, and then an image-based alveolar model, obtained from micro-CT images of rat lung parenchyma (Concha & Hurtado, 2020). The objective of these models is to observe how simplifications on the geometry affect the micromechanical response, such as the stress distribution within the RVE, or the presence of local phenomena. In both cases two load patterns will be analyzed, first a pressure-driven RVE, with a uniform pore pressure in the cavity and with the macroscopic strain as a variable of the problem, i.e., the model described in the previous section, and then in a deformation-driven setting, removing the pore pressure and applying an equivalent macroscopic strain (obtained from the solution to the first case). Both loading conditions intend to represent, in an approximate way, physiological conditions in the pulmonary tissue. The pressure-driven model resembles the tissue conditions under mechanical ventilation, where the respiratory muscles are passive and the pressure generated by the ventilator drives the air into the lungs (Mauri et al., 2017), and the deformation-driven mimics spontaneous breathing, where the respiratory muscles have an active role. In all cases, we will compare the three kinematical constraints (KUBC, PBC and SUBC) in terms of the stress distributions.

For the lung parenchyma mechanical behavior, we select an incompressible neo-Hookean strain energy function, with an elastic modulus set to $E = 95$ kPa according to the values reported by Perlman and Wu (2014), which is equivalent to $\mu = \frac{E}{2(1+\nu)} = 31.7$ kPa, using a Poisson ratio $\nu = 0.5$. It is worth noting that other phenomenological strain energy functions have been studied for the representation of the behavior of lung parenchyma in the literature (Bel-Brunon et al., 2014; Birzle et al., 2019; Birzle & Wall, 2019). However, in

this work we choose the neo-Hookean model to minimize the number of material parameters and the non-linearity of the material model, and concentrate on the effect of boundary conditions and microstructural geometry. The RVE is loaded using a positive pore pressure ranging from $p_0 = 0$ to 1.962 kPa. The numerical simulations were carried out using the FEniCS library for finite element computations (Logg et al., 2012). To account for the incompressible behavior of the solid phase, we considered a mixed FE formulation that employs P_2 - P_1 Taylor-Hood tetrahedral elements.

2.3.1. Spherical alveolar model

In the literature, the complex lung parenchyma microstructure has been simplified using polyhedral representations (Concha et al., 2018; Fung, 1988; Koshiyama & Wada, 2015; Roth et al., 2017; Warren & Kraynik, 1997). However, as in this work the main objective of the numerical simulations is to illustrate the application of the model described in the previous section, and not necessarily present a detailed study of the tissue behavior, here we will use a geometry consisting of a spherical cavity embedded in a homogeneous matrix, that represents a large spherical alveolus. The mesh was constructed using GMSH (Geuzaine & Remacle, 2009), with special care to make the external boundary periodic (requisite for the PBC); specifically, it consists in a cube of edge size $122.5 \mu\text{m}$ (the same size as the image-based RVE that will be studied) with an internal spherical cavity that intersects the cube boundaries, as shown in Figure 2.1b. The cavity radius is such that the porosity of the RVEs of the spherical and image-based alveolar models be similar, with the porosity in the reference configuration defined as $f_0 := |\Omega_0^F|/|\Omega_0|$, which in this case gives 63.24% (versus 63.22% for the image-based RVE of figure 2.1c). We remark that, while both geometries have similar porosity, the single alveolus model considers a uniform smooth cavity, which is clearly different from the intricate microstructure observed in micro-CT images of alveolar tissue. A measure of this difference is the surface-to-volume ratio, that if defined as the area of the inner surface $\partial\Omega_0^N$ divided by the volume of gas in the RVE, gives a value of $0.0356 \mu\text{m}^{-1}$ for the spherical model and $0.1032 \mu\text{m}^{-1}$ for the image-based case (see Section 2.3.2).

To compare the performance of the different kinematical constraints, we use two scalar stress measures: the hydrostatic stress, related with the first invariant of the Cauchy stress tensor,

$$\sigma_{\text{hyd}} := \frac{1}{3}\text{trace}(\boldsymbol{\sigma}), \quad (2.35)$$

and the von Mises stress,

$$\sigma_{\text{VM}} := \sqrt{\frac{3}{2}\boldsymbol{\sigma}_{\text{dev}} : \boldsymbol{\sigma}_{\text{dev}}}, \quad (2.36)$$

that is related to shear stresses, and where the deviatoric component of the stress tensor is

$$\boldsymbol{\sigma}_{\text{dev}} := \boldsymbol{\sigma} - \sigma_{\text{hyd}}\mathbf{I}. \quad (2.37)$$

From these definitions, we note that the hydrostatic and the von Mises stress quantify two independent and orthogonal components of the Cauchy stress tensor.

Figures 2.2 and 2.3 show the hydrostatic and von Mises stress for a pore pressure of 1.962 kPa, respectively. As the Cauchy stress tensor is defined in the current configuration, in these Figures the quantities are plotted in the deformed state. For the hydrostatic stress, the RVE exhibits a response that depends on the kinematical constraint and the type of loading. While for the KUBC there are peak values near the cube edges, in the SUBC there are peaks near the sphere edges (where it intersects the cube faces), especially noticeable in the deformation-driven case. For the von Mises stress, the distribution is independent of the type of loading. However, it depends on the kinematical constraint: in the KUBC there are smaller values, in the SUBC there are peaks in the sphere edges and the PBC response is similar to the SUBC but without these peak values.

The stress distributions plotted in the current configuration allow observing the distributions, if there are peak values and where they are located, however, for a more detailed comparison, in Figure 2.4 the frequency distributions of the hydrostatic and von Mises stress are presented. To facilitate the comparison, in these figures the curves were done using the `gaussian_kde` function available in `SciPy` (Virtanen et al., 2020), which produce a kernel-density estimate using Gaussian kernels. The results show that for the

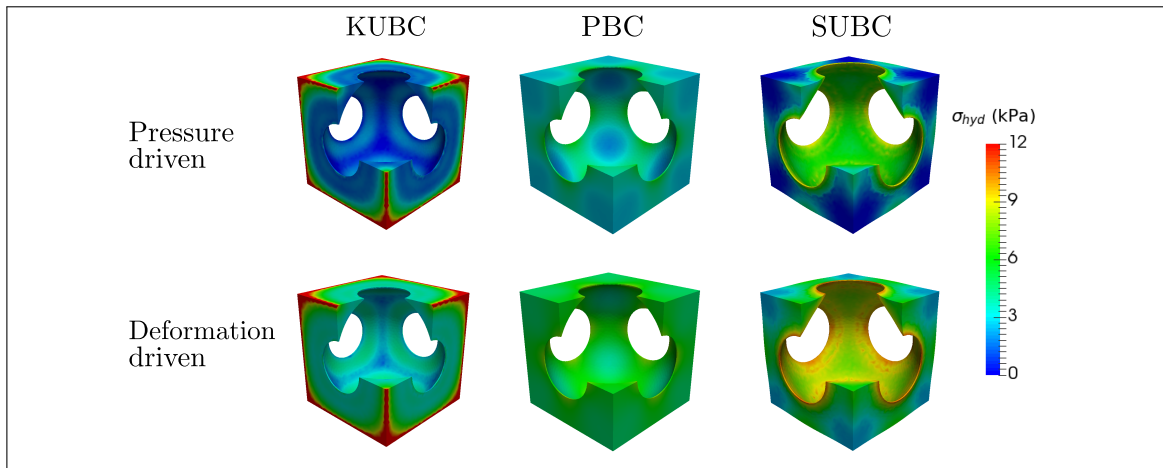


Figure 2.2. Hydrostatic stress field in the spherical alveolar model, plotted in the current configuration.

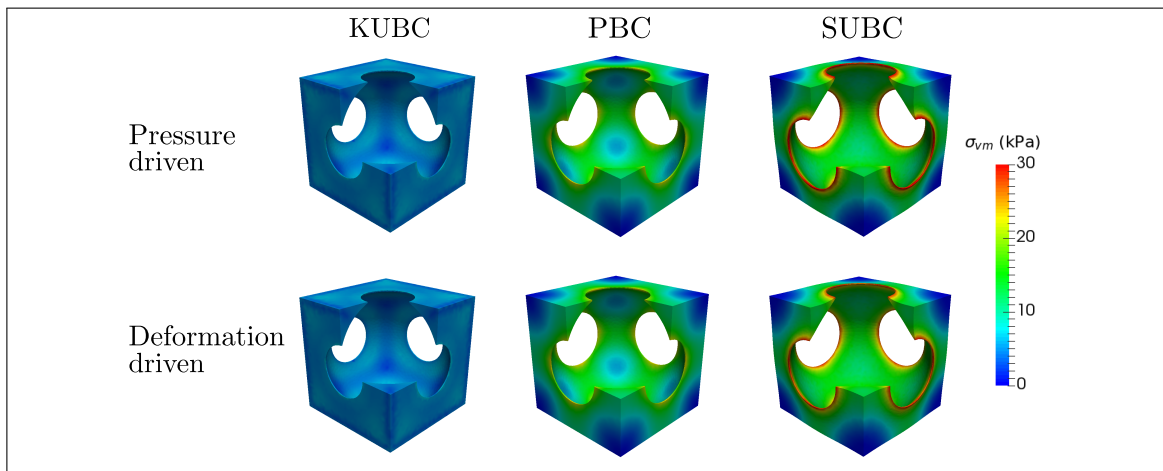


Figure 2.3. Von Mises stress field in the spherical alveolar model, plotted in the current configuration.

hydrostatic stress, the three kinematical constraints produce different distributions, but for each case, when the macrostrain is given instead of applying a pore pressure (i.e., deformation-driven instead of pressure-driven), there is a shift in the distributions, with higher values but the same shape. For the von Mises stress, the distribution in the PBC and SUBC are similar, in agreement with the observed in Figure 2.3, while the KUBC exhibits lower and more concentrated values. Additionally, for the KUBC and PBC the distribution

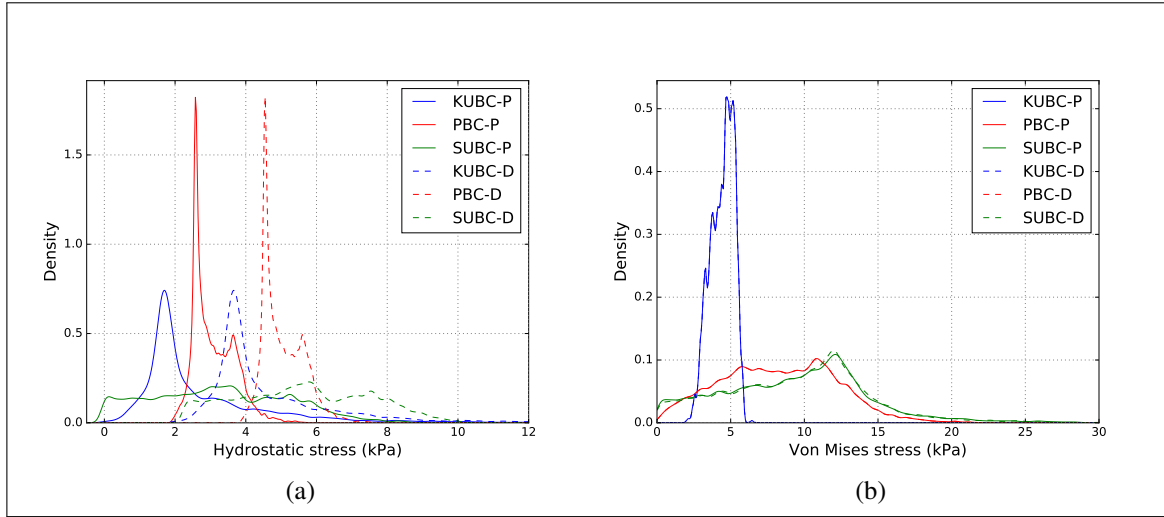


Figure 2.4. Spherical alveolar model, distributions for (a) hydrostatic stress, and (b) von Mises stress. The values depend on the kinematical constraint selected: KUBC (blue), PBC (red) and SUBC (green), and in the type of loading: pressure-driven in solid lines, deformation-driven in dashed lines. For each kinematical constraint, the removal of the pore pressure and application of an equivalent macrostrain, produces a shift in the hydrostatic stress, while the von Mises stress remains constant with the KUBC and PBC, and has slight differences with the SUBC.

is indistinguishable for both loadings (pressure-driven in solid lines, deformation-driven in dashed lines), while for the SUBC there is a slight difference between 10 and 15 kPa, that is not noticeable in the plots of Figure 2.3.

2.3.2. Image-based alveolar model

For the image-based alveolar model, a cuboid RVE of edge size $122.5 \mu\text{m}$ is selected from micro-CT images of rat lung parenchyma previously reported by our group (Concha et al., 2018; Sarabia-Vallejos et al., 2019). The RVE preserves the morphological features of the alveolated tissue; however, due to the natural heterogeneities the resulting mesh is not periodic, hindering the straight use of PBC. To overcome this issue different methods have been proposed, for example Pahr and Zysset (2008) used a perfectly periodic mirrored mesh of cancellous bone (obtained by reflecting successively the original mesh

in the x , y and z directions). To avoid the need of matching meshes on opposite RVE boundaries, Larsson et al. (2011) weakly imposed the fluctuation periodicity (and traction anti-periodicity), and Nguyen et al. (2012) developed a method based on polynomial interpolation of the displacement in the boundaries. In this paper, following the straightforward approach of the mirrored mesh, the original RVE (Figure 2.1c) is reflected, obtaining the geometry shown in Figure 2.5, a cube of edge size $245 \mu\text{m}$, which is easy to obtain but that is not a completely realistic structure and has eight times the number of elements of the original mesh.

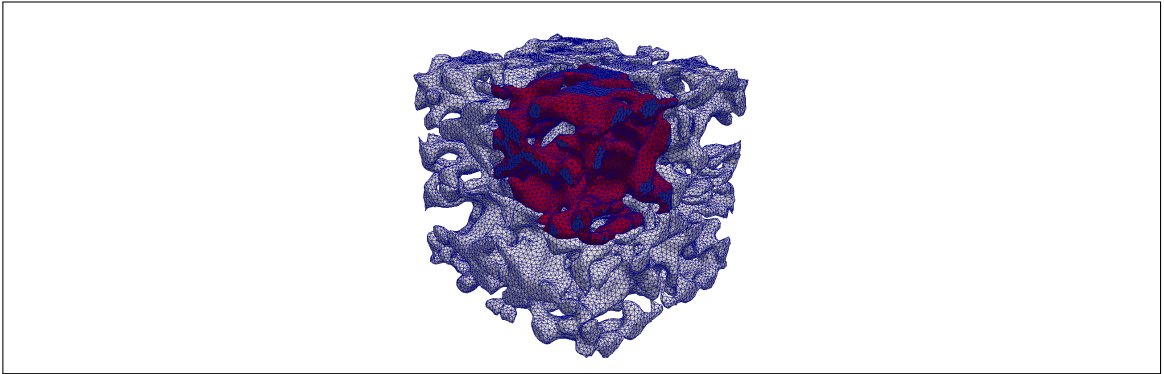


Figure 2.5. The mesh of the image-based alveolar model obtained by micro-CT images is not periodic (due to natural heterogeneities in the tissue), so in order to apply the PBC the original mesh (in red) is reflected successively in the x , y and z directions, obtaining a perfectly periodic mesh (in gray).

Analogous to the spherical alveolar model, we plot the hydrostatic and von Mises stress distributions, which are shown in Figures 2.6 and 2.7. In this case, we see that for both measures, the stress values are similar with the KUBC, PBC and SUBC constraints, except for some values in the exterior boundary, particularly around the upper right corner of the deformed RVE, where a thin “bar” of tissue has higher stress values with the SUBC and lower values with the KUBC.

Consistent with the plots of Figure 2.6, the results reported in Figure 2.8a show that the hydrostatic stress distributions are similar for the three kinematical constraints. In effect, in the pressure-driven case, the KUBC, PBC and SUBC models result in a peak

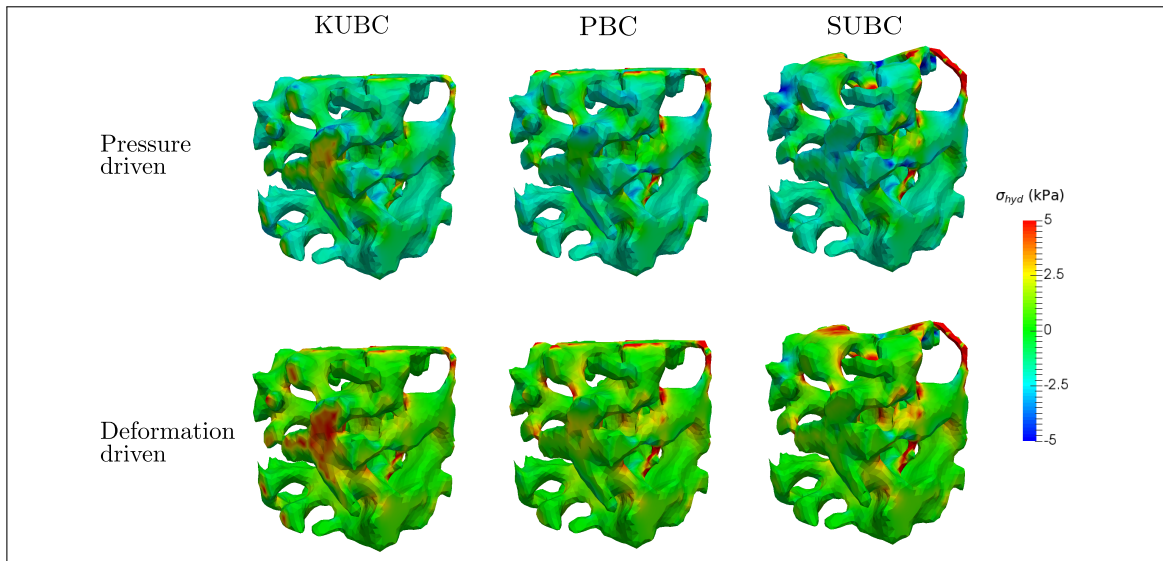


Figure 2.6. Hydrostatic stress field in the image-based alveolar model, plotted in the current configuration.

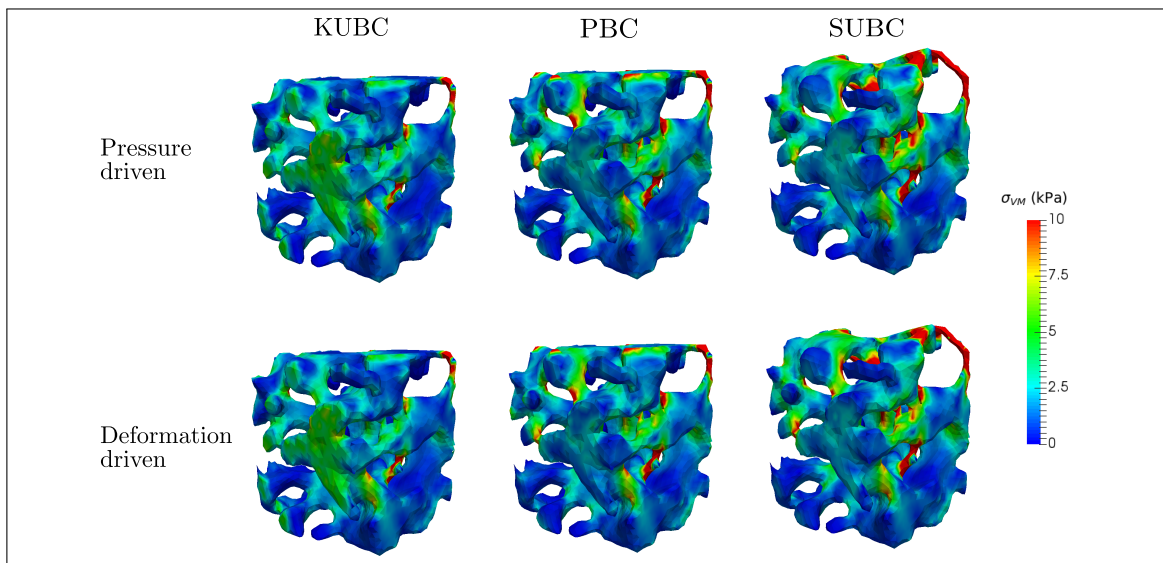


Figure 2.7. Von Mises stress field in the image-based alveolar model, plotted in the current configuration.

that occurs close to the pore pressure (1.96 kPa). Interestingly, in the deformation-driven case, the shape of the stress distributions are similar to those observed in the pressure-driven setting, only shifted towards the positive values with the peak occurring near 0 kPa.

Regarding the von Mises stress, there are virtually no differences between the pressure- and deformation-driven cases, see Figure 2.8b. Further, all distributions are unimodal, with the KUBC and PBC giving similar values, and the SUBC slightly higher values.

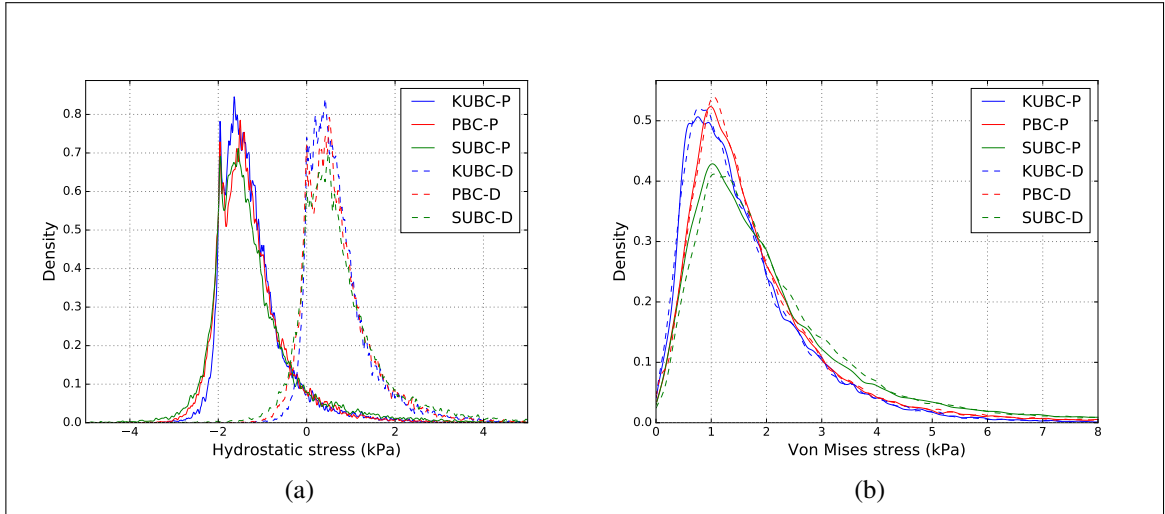


Figure 2.8. Image-based alveolar model, distributions for (a) hydrostatic stress, and (b) von Mises stress. The Figure shows the results with each kinematical constraint: KUBC (blue), PBC (red) and SUBC (green); and type of loading: pressure-driven in solid lines, deformation-driven in dashed lines. For both stress measures, the shape of the distributions is similar for the different kinematical constraints. Also, the removal of the pore pressure and application of an equivalent macrostrain, produces a shift in the hydrostatic stress, while the von Mises stress remains similar.

While the focus of this work is on the micromechanical behavior, the macroscopic (averaged) response constitutes a useful measure to compare the different kinematical constraints and to observe how they affect the global values. Then, in order to compare the different cases studied at a macro-perspective, in Appendix C we show the values of the macroscopic strain and stress.

2.4. Discussion

In this work, we propose a variational framework for the micromechanical response of OCFs. We employ the framework in the analysis of the micromechanical behavior under

pressure-driven conditions, where we consider a spherical alveolar and an image-based alveolar models to assess the stress distributions. For each geometry considered, three different boundary conditions were studied. One key conclusion is that both the hydrostatic and deviatoric stress distributions in the spherical alveolar model were highly dependent on the boundary condition assumed for the micromechanical analysis, see Figure 2.4. In effect, the peak values of the distributions did not coincide, and there was no clear trend in terms of modality of the distribution. In contrast, when looking at image-based alveolar model, all three boundary conditions resulted in virtually the same stress distribution, see Figure 2.8. In particular, the hydrostatic distribution displayed a bimodal shape, whereas the von Mises stress showed positively-skewed unimodal distribution. To facilitate a comparison between the spherical and image-based alveolar models, we have summarized the stress distributions in terms of box and whisker plots, see Figure 2.9. We observe that in the case of image-based alveolar model, all boundary conditions lead to consistent stress distributions, which is not the case for the spherical model. We further note that the results for the image-based model are consistent with stress distributions reported in previous works, where alveolar geometries obtained from micro-CT images under varying levels of alveolar pressure were analyzed (Sarabia-Vallejos et al., 2019). In those simulations, boundary conditions were arbitrarily chosen, not based on theoretical grounds. The resulting hydrostatic and deviatoric stress distributions in that work are very similar in shape to those shown in Figure 2.8. Interestingly, in this work we have shown that in anatomical geometries, the conditions imposed on the boundary do not seem to play a key role in the micromechanical response. A possible explanation for this behavior is the random unstructured trabecular geometry of the alveolated pulmonary tissue, that quickly dissipates stress localizations that may arise at the boundaries of the RVE due to different conditions, see Figures 2.6 and 2.7. From these results, we conclude that, while two RVE may have similar macroscopic properties such as global porosity, their microstructural stresses can strongly differ. Further, stresses in randomly-structured RVEs do not seem affected by the boundary conditions, whereas highly structured RVEs do.

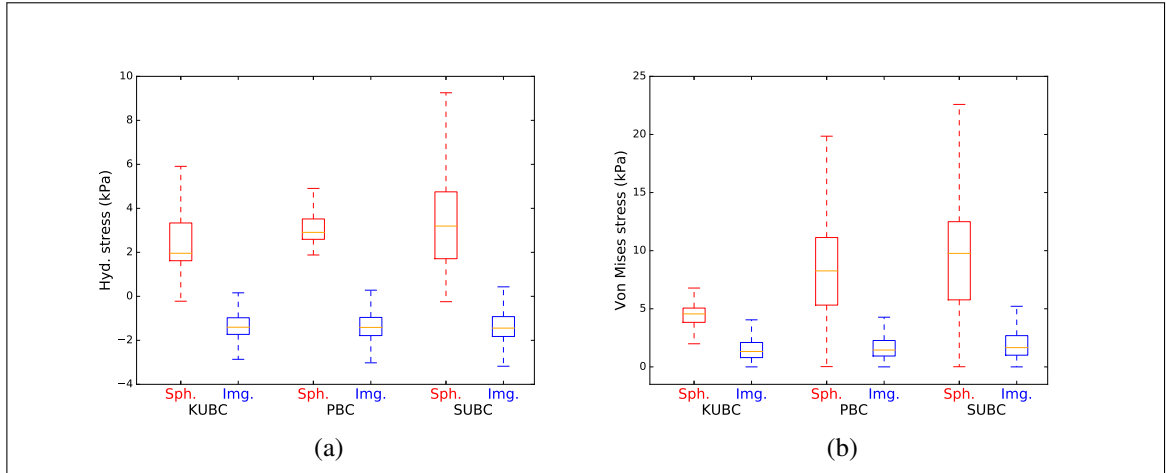


Figure 2.9. Comparison of the (a) hydrostatic and (b) von Mises stress distributions for the pressure-driven RVE, with the spherical and image-based alveolar models, in red and blue boxes, respectively. The boxes range from the lower (Q_1) to upper (Q_3) quartile values of the stress, with a line at the median. The whiskers extend from the boxes to show the range of the data. The upper whiskers extend to the last value less than $Q_3 + 1.5 \text{ IQR}$, while the lower whiskers to the first value greater than $Q_1 - 1.5 \text{ IQR}$, where $\text{IQR} = Q_3 - Q_1$ is the interquartile range. The outliers are not shown for clarity.

To understand the differences between formulations where either pressure or deformation is imposed, we consider models where boundary conditions are driven by a macroscopic deformation \bar{U} under zero pore pressure. The results in both the spherical and image-based alveolar models (Figures 2.4 and 2.8, respectively) show that the hydrostatic stress distributions are shifted between the pressure-driven and the deformation-driven cases, while the von Mises stress distributions remain the same. Interestingly, in the deformation-driven case we observe that boundary conditions do affect the spherical model distribution of stress in a way similar to the pressure-driven case. However, the results for the deformation-driven image-based model show that the choice of boundary conditions does not influence the stress distribution, resembling the behavior observed in the pressure-driven case. We remark that the shift in the hydrostatic stresses in finite deformation poro-elasticity has been addressed by Idiart and Lopez-Pamies (2012), borrowing ideas from Julien et al. (2011) and Vincent et al. (2009). In their work, Idiart &

Lopez-Pamies showed that stresses in an incompressible elastomeric solid with pressurized closed cavities can be expressed as

$$\bar{\mathbf{P}} = \tilde{\mathbf{P}} - p_0 J \mathbf{F}^{-T}, \quad (2.38)$$

where $\tilde{\mathbf{P}}$ corresponds to the first Piola-Kirchhoff stress tensor obtained from solving the same microstructure subject to an equivalent macroscopic strain and zero pore pressure, and p_0 corresponds to the pressure applied in the closed cavities. In the current configuration, Equation 2.38 is equivalent to adding a hydrostatic pressure term with magnitude p_0 to the Cauchy stress tensor, which explains the shift in the hydrostatic stress distribution. Since the cavity pressure effect only results in an isotropic tensor, the von Mises stress remains the same under this transformation. In Idiart and Lopez-Pamies (2012), to find the equivalent macroscopic strain, an additional equation is imposed, which is based on the traction-free condition on the external boundary, and consists in making zero the average of the first Piola-Kirchhoff stress tensor in the entire RVE (solid and fluid domain). Interestingly, under the same assumptions (a closed-cell composite and extending $\tilde{\mathbf{P}}$ to the fluid domain) and with some algebraic manipulations, this equation can be related to the stationary condition Equation (2.16), which is generated by considering the macroscopic strain as a variable of the problem. The relationship between pressure-driven and deformation-driven formulations has profound consequences on the modeling of free-breathing versus ventilated-breathing, for instance in the context of lung mechanical simulations (Hurtado et al., 2020; Patte et al., 2020; Patte et al., 2019; Tawhai & Lin, 2010).

The present work can be expanded in several directions. First, we note that the choice of a neo-Hookean strain energy function imposes an important limitation when studying OCFs, which may exhibit a strongly non-linear mechanical behavior (for lung parenchyma, see Bel-Brunon et al. (2014), Birzle et al. (2019), and Birzle and Wall (2019)). In this work we chose a simple constitutive law to isolate its effect on the results, allowing us to better focus on assessing the impact of boundary conditions and geometry on the RVE stress distribution and response. Future contributions should incorporate other constitutive relations that are specific to the material under analysis, and that may exhibit

other type of mechanical behavior, e.g. viscoelastic and hysteretic response (West, 2012). This, in turn, may necessitate an extension of the current variational framework, which has been developed under the assumption of a material with hyperelastic response. Another limitation is the lack of experimental validation of the results obtained from numerical simulations. Micro-CT imaging combined with digital image correlation has been used to assess the deformation fields arising in bone samples under compressive loading (Dickinson et al., 2011), allowing for the validation of FE simulations of bone microstructures (Hambli, 2013). We note, however, that the validation of pressurized porous materials may require more sophisticated setups that maintain the applied pressure in sealed samples, which may not be compatible with current micro-CT technologies.

Acknowledgements

This work was funded by the National Agency for Research and Development (ANID) of Chile through the grant FONDECYT Regular # 1180832.

3. CONCLUSIONS

In this thesis, a variational framework for the micromechanical analysis of pressure-driven porous materials is formulated. The proposed model is applied in numerical simulations in the context of lung micromechanics, first with a spherical alveolar model and then with an image-based alveolar model. In the first case, the hydrostatic and von Mises stress distributions are highly dependent on the kinematical constraints. Conversely, in the image-based model, the stress distributions are the same for all constraints, and only slight differences were observed in the stress values near the external boundary. Additionally, these results show that even if two RVEs have similar macroscopic properties, such as the global porosity, and the solid has the same strain energy function, the microstructural stresses can differ. The stresses can even have an opposite sign (for the pressure-driven simulations, the hydrostatic stress values are positive in the spherical model, while in the image-based model, they are predominantly negative).

For the loading of the RVE, in addition to the pressure-driven setting, a set of deformation-driven simulations were performed, with a given macroscopic strain (obtained as a result of the previous case) and zero pore pressure. The results show that for each constraint, the hydrostatic stress distribution is shifted between both loading settings, while the von Mises stress values remain similar. Moreover, the pressure-driven and deformation-driven simulations of the lung parenchyma can be related to mechanical ventilation and spontaneous breathing, respectively, giving an insight into the differences between both states.

4. PERSPECTIVES

In this thesis, the proposed model for pressure-driven foams is applied in the context of lung parenchyma simulations; however, it can be used to understand and model different kinds of foams with pressurized cavities. Examples of areas where the pore pressure plays a key role, and our model could be of interest, are the shrinkage of expanded polystyrene after demolding (Fen-Chong et al., 1999), cavitation and fracture of hydrogels (Kundu & Crosby, 2009) and internal fracture of rubber materials when high-pressure gases are suddenly decompressed (Yamabe et al., 2011).

For the lung parenchyma simulations, a neo-Hookean strain energy function was selected. However, the tissue has a viscoelastic and nonlinear response (Bel-Brunon et al., 2014; Birzle et al., 2019; Birzle & Wall, 2019), which is not captured correctly by a neo-Hookean function. Additionally, other compounds also affect the mechanical response, such as the pulmonary surfactant, that contributes to the hysteresis and alveoli stability (West, 2012). Therefore, to find proper conclusions about the tissue response, future studies should incorporate these conditions.

This thesis's main topic is pressure-driven RVEs; nonetheless, other states can be related to this condition. For example, thermo-mechanical simulations where a change in the temperature produces the deformation, as done to obtain the effective thermal expansion coefficients of composites (Akulichev et al., 2016; Karch, 2014). The framework proposed here can be adapted to study this situation, keeping the macroscopic strain as a variable of the problem and setting the temperature increment as the loading (instead of the pore pressure, as discussed here). Then, from the displacements found, the coefficients can be computed directly.

BIBLIOGRAPHY

Akulichev, A. G., Alcock, B., Tiwari, A., & Echtermeyer, A. T. (2016). Thermomechanical properties of zirconium tungstate/hydrogenated nitrile butadiene rubber (HNBR) composites for low-temperature applications. *Journal of Materials Science*, *51*(24), 10714–10726. <https://doi.org/10.1007/s10853-016-0236-6>

Altenbach, H., & Öchsner, A. (Eds.). (2010). *Cellular and porous materials in structures and processes*. Springer Science & Business Media.

Bakhvalov, N., & Panasenko, G. (1989). *Homogenization: averaging processes in periodic media*. Dordrecht, The Netherlands, Kluwer Academic Publishers. [https://doi.org/10.1016/0378-4754\(90\)90168-i](https://doi.org/10.1016/0378-4754(90)90168-i)

Bargmann, S., Klusemann, B., Markmann, J., Schnabel, J. E., Schneider, K., Soyarslan, C., & Wilmers, J. (2018). Generation of 3D representative volume elements for heterogeneous materials: A review. *Progress in Materials Science*, *96*, 322–384. <https://doi.org/10.1016/j.pmatsci.2018.02.003>

Bednarczyk, B. A., Aboudi, J., Arnold, S. M., & Sullivan, R. M. (2008). Analysis of Space Shuttle external tank spray-on foam insulation with internal pore pressure. *Journal of Engineering Materials and Technology, Transactions of the ASME*, *130*(4). <https://doi.org/10.1115/1.2969247>

Bel-Brunon, A., Kehl, S., Martin, C., Uhlig, S., & Wall, W. A. (2014). Numerical identification method for the non-linear viscoelastic compressible behavior of soft tissue using uniaxial tensile tests and image registration - Application to rat lung parenchyma. *Journal of the Mechanical Behavior of Biomedical Materials*, *29*, 360–374. <https://doi.org/10.1016/j.jmbbm.2013.09.018>

- Biot, M. A. (1941). General theory of three-dimensional consolidation. *Journal of Applied Physics*, *12*(2), 155–164. <https://doi.org/10.1063/1.1712886>
- Birzle, A. M., Hobrack, S. M., Martin, C., Uhlig, S., & Wall, W. A. (2019). Constituent-specific material behavior of soft biological tissue: experimental quantification and numerical identification for lung parenchyma. *Biomechanics and Modeling in Mechanobiology*, *18*(5), 1383–1400. <https://doi.org/10.1007/s10237-019-01151-3>
- Birzle, A. M., & Wall, W. A. (2019). A viscoelastic nonlinear compressible material model of lung parenchyma - Experiments and numerical identification. *Journal of the Mechanical Behavior of Biomedical Materials*, *94*, 164–175. <https://doi.org/10.1016/j.jmbbm.2019.02.024>
- Bonet, J., & Wood, R. D. (1997). *Nonlinear continuum mechanics for finite element analysis*. Cambridge University Press. <https://doi.org/10.1017/CBO9780511755446>
- Cao, T. S., Maire, E., Verdu, C., Bobadilla, C., Lasne, P., Montmitonnet, P., & Bouchard, P. O. (2014). Characterization of ductile damage for a high carbon steel using 3D X-ray micro-tomography and mechanical tests - Application to the identification of a shear modified GTN model. *Computational Materials Science*, *84*, 175–187. <https://doi.org/10.1016/j.commatsci.2013.12.006>
- Carniel, T. A., Klahr, B., & Fancello, E. A. (2019). On multiscale boundary conditions in the computational homogenization of an RVE of tendon fascicles. *Journal of the Mechanical Behavior of Biomedical Materials*, *91*, 131–138. <https://doi.org/10.1016/j.jmbbm.2018.12.003>
- Chapelle, D., & Moireau, P. (2014). General coupling of porous flows and hyperelastic formulations - From thermodynamics principles to energy balance and compatible time schemes. *European Journal of Mechanics, B/Fluids*, *46*, 82–96. <https://doi.org/10.1016/j.euromechflu.2014.02.009>

Collis, J., Brown, D. L., Hubbard, M. E., & O’Dea, R. D. (2017). Effective equations governing an active poroelastic medium. *Proceedings of the Royal Society A: Mathematical, Physical and Engineering Sciences*, 473(2198), 20160755. <https://doi.org/10.1098/rspa.2016.0755>

Concha, F., & Hurtado, D. E. (2020). Upscaling the poroelastic behavior of the lung parenchyma: A finite-deformation micromechanical model. *Journal of the Mechanics and Physics of Solids*, 145, 104147. <https://doi.org/10.1016/j.jmps.2020.104147>

Concha, F., Sarabia-Vallejos, M., & Hurtado, D. E. (2018). Micromechanical model of lung parenchyma hyperelasticity. *Journal of the Mechanics and Physics of Solids*, 112, 126–144. <https://doi.org/10.1016/j.jmps.2017.11.021>

Coussy, O. (2004). *Poromechanics*. Chichester, England, John Wiley & Sons.

De Souza Neto, E., & Feijóo, R. (2006). Variational foundations of multi-scale constitutive models of solid: Small and large strain kinematical formulation. *LNCC Research & Development Report*, 16. <https://doi.org/10.1002/9783527632312.ch9>

Deville, S., Saiz, E., Nalla, R. K., & Tomsia, A. P. (2006). Freezing as a path to build complex composites. *Science*, 311(5760), 515–518.

Dickinson, A. S., Taylor, A. C., Ozturk, H., & Browne, M. (2011). Experimental validation of a finite element model of the proximal femur using digital image correlation and a composite bone model. *Journal of Biomechanical Engineering*, 133(1). <https://doi.org/10.1115/1.4003129>

Dormieux, L., Molinari, A., & Kondo, D. (2002). Micromechanical approach to the behavior of poroelastic materials. *Journal of the Mechanics and Physics of Solids*, 50(10), 2203–2231. [https://doi.org/10.1016/S0022-5096\(02\)00008-X](https://doi.org/10.1016/S0022-5096(02)00008-X)

Evans, L. (1998). *Partial Differential Equations*. American Mathematical Society.

Fen-Chong, T., Hervé, E., & Zaoui, A. (1999). Micromechanical modelling of intracellular pressure-induced viscoelastic shrinkage of foams: Application to expanded polystyrene. *European Journal of Mechanics - A/Solids*, 18(2), 201–218. [https://doi.org/10.1016/S0997-7538\(99\)80012-6](https://doi.org/10.1016/S0997-7538(99)80012-6)

Fish, J. (2013). *Practical multiscale*. John Wiley & Sons. <https://doi.org/10.1007/978-94-009-3489-4>

Fung, Y. C. (1988). A model of the lung structure and its validation. *Journal of Applied Physiology*, 64(5), 2132–2141. <https://doi.org/10.1152/jappl.1988.64.5.2132>

Genet, M., Couégnat, G., Tomsia, A. P., & Ritchie, R. O. (2014). Scaling strength distributions in quasi-brittle materials from micro-to macro-scales: A computational approach to modeling nature-inspired structural ceramics. *Journal of the Mechanics and Physics of Solids*, 68, 93–106.

Geuzaine, C., & Remacle, J. F. (2009). Gmsh: A 3-D finite element mesh generator with built-in pre- and post-processing facilities. *International Journal for Numerical Methods in Engineering*, 79(11), 1309–1331. <https://doi.org/10.1002/nme.2579>

Gibson, L. J., & Ashby, M. F. (1997). *Cellular solids: Structure and properties*. Cambridge, UK, Cambridge University Press. <https://doi.org/10.1017/CBO9781139878326>

Guo, L., Vardakis, J. C., Chou, D., & Ventikos, Y. (2020). A multiple-network poroelastic model for biological systems and application to subject-specific modelling of cerebral fluid transport. *International Journal of Engineering Science*, 147, 103204.

Hambli, R. (2013). Micro-CT finite element model and experimental validation of trabecular bone damage and fracture. *Bone*, 56(2), 363–374. <https://doi.org/10.1016/j.bone.2013.06.028>

Hannard, F., Pardoën, T., Maire, E., Le Bourlot, C., Mokso, R., & Simar, A. (2016). Characterization and micromechanical modelling of microstructural heterogeneity effects on

ductile fracture of 6xxx aluminium alloys. *Acta Materialia*, 103, 558–572. <https://doi.org/10.1016/j.actamat.2015.10.008>

Hashin, Z. (1983). Analysis of composite materials-a survey. *Journal of Applied Mechanics*, 50(3), 481–505. <https://doi.org/10.1115/1.3167081>

Hill, R. (1963). Elastic properties of reinforced solids: Some theoretical principles. *Journal of the Mechanics and Physics of Solids*, 11(5), 357–372. [https://doi.org/10.1016/0022-5096\(63\)90036-X](https://doi.org/10.1016/0022-5096(63)90036-X)

Hill, R. (1972). On constitutive macro-variables for heterogeneous solids at finite strain. *Proceedings of the Royal Society of London. A. Mathematical and Physical Sciences*, 326(1565), 131–147. <https://doi.org/10.1098/rspa.1972.0001>

Hollister, S. J., & Kikuchi, N. (1992). A comparison of homogenization and standard mechanics analyses for periodic porous composites. *Computational Mechanics*, 10(2), 73–95. <https://doi.org/10.1007/BF00369853>

Holzapfel, G. (2000). *Nonlinear Solid Mechanics: A Continuum Approach for Engineering*. Chichester, John Wiley & Sons. <https://doi.org/10.1023/A:1020843529530>

Houmard, M., Fu, Q., Genet, M., Saiz, E., & Tomsia, A. P. (2013). On the structural, mechanical, and biodegradation properties of HA/ β -TCP robocast scaffolds. *Journal of Biomedical Materials Research Part B: Applied Biomaterials*, 101(7), 1233–1242.

Huet, C. (1990). Application of variational concepts to size effects in elastic heterogeneous bodies. *Journal of the Mechanics and Physics of Solids*, 38(6), 813–841. [https://doi.org/10.1016/0022-5096\(90\)90041-2](https://doi.org/10.1016/0022-5096(90)90041-2)

Hurtado, D. E., Erranz, B., Lillo, F., Sarabia-Vallejos, M., Iturrieta, P., Morales, F., Blaha, K., Medina, T., Diaz, F., & Cruces, P. (2020). Progression of regional lung strain and heterogeneity in lung injury: assessing the evolution under spontaneous breathing and mechanical ventilation. *Annals of Intensive Care*, 10, 107.

Idiart, M. I., & Lopez-Pamies, O. (2012). On the overall response of elastomeric solids with pressurized cavities. *Comptes Rendus - Mecanique*, 340((4-5)), 359–368. <https://doi.org/10.1016/j.crme.2012.02.018>

Javili, A., Saeb, S., & Steinmann, P. (2017). Aspects of implementing constant traction boundary conditions in computational homogenization via semi-Dirichlet boundary conditions. *Computational Mechanics*, 59(1), 21–35.

Ju, F., Xia, Z., & Sasaki, K. (2008). On the finite element modelling of balloon-expandable stents. *Journal of the Mechanical Behavior of Biomedical Materials*, 1(1), 86–95. <https://doi.org/10.1016/j.jmbbm.2007.07.002>

Julien, J., Garajeu, M., & Michel, J. C. (2011). A semi-analytical model for the behavior of saturated viscoplastic materials containing two populations of voids of different sizes. *International Journal of Solids and Structures*, 48(10), 1485–1498. <https://doi.org/10.1016/j.ijsolstr.2011.01.031>

Kanit, T., Forest, S., Galliet, I., Mounoury, V., & Jeulin, D. (2003). Determination of the size of the representative volume element for random composites: Statistical and numerical approach. *International Journal of Solids and Structures*, 40(13-14), 3647–3679. [https://doi.org/10.1016/S0020-7683\(03\)00143-4](https://doi.org/10.1016/S0020-7683(03)00143-4)

Kantzos, C. A., Cunningham, R. W., Tari, V., & Rollett, A. D. (2018). Characterization of metal additive manufacturing surfaces using synchrotron X-ray CT and micromechanical modeling. *Computational Mechanics*, 61(5), 575–580. <https://doi.org/10.1007/s00466-017-1531-z>

Karch, C. (2014). Micromechanical Analysis of Thermal Expansion Coefficients. *Modeling and Numerical Simulation of Material Science*, 2014(4), 104–118. <https://doi.org/10.4236/mnsms.2014.43012>

Koshiyama, K., Nishimoto, K., Ii, S., Sera, T., & Wada, S. (2019). Heterogeneous structure and surface tension effects on mechanical response in pulmonary acinus: A finite element analysis. *Clinical Biomechanics*, *66*, 32–39. <https://doi.org/10.1016/j.clinbiomech.2018.01.001>

Koshiyama, K., & Wada, S. (2015). Mathematical model of a heterogeneous pulmonary acinus structure. *Computers in Biology and Medicine*, *62*, 25–32. <https://doi.org/10.1016/j.combiomed.2015.03.032>

Kundu, S., & Crosby, A. J. (2009). Cavitation and fracture behavior of polyacrylamide hydrogels. *Soft Matter*, *5*(20), 3963–3968. <https://doi.org/10.1039/b909237d>

Larsson, F., Runesson, K., Saroukhani, S., & Vafadari, R. (2011). Computational homogenization based on a weak form of micro-periodicity for RVE-problems. *Computer Methods in Applied Mechanics and Engineering*, *200*(1-4), 11–26. <https://doi.org/10.1016/j.cma.2010.06.023>

Liu, M., & Chen, C. (2015). A micromechanical analysis of the fracture properties of saturated porous media. *International Journal of Solids and Structures*, *63*, 32–38. <https://doi.org/10.1016/j.ijsolstr.2015.02.031>

Logg, A., Mardal, K. A., & Wells, G. N. (Eds.). (2012). *Automated Solution of Differential Equations by the Finite Element Method*. Springer. https://doi.org/10.1007/978-3-642-23099-8_1

Ma, L., Rolfe, B. F., Yang, Q., & Yang, C. (2011). The configuration evolution and macroscopic elasticity of fluid-filled closed cell composites: Micromechanics and multiscale homogenization modelling. *CMES - Computer Modeling in Engineering and Sciences*, *79*(2), 131–158.

Ma, L., & Yang, Q. (2018). Micromechanics-based elastic fields of closed-cell porous media. *CMES - Computer Modeling in Engineering and Sciences*, 114(2), 239–259. <https://doi.org/10.3970/cmcs.2018.114.239>

Mauri, T., Cambiaghi, B., Spinelli, E., Langer, T., & Grasselli, G. (2017). Spontaneous breathing: A double-edged sword to handle with care. *Annals of Translational Medicine*, 5(14). <https://doi.org/10.21037/atm.2017.06.55>

Nguyen, V. D., Béchet, E., Geuzaine, C., & Noels, L. (2012). Imposing periodic boundary condition on arbitrary meshes by polynomial interpolation. *Computational Materials Science*, 55, 390–406. <https://doi.org/10.1016/j.commatsci.2011.10.017>

Ogden, R. W. (1974). On the overall moduli of non-linear elastic composite materials. *Journal of the Mechanics and Physics of Solids*, 22(6), 541–553. [https://doi.org/10.1016/0022-5096\(74\)90033-7](https://doi.org/10.1016/0022-5096(74)90033-7)

Pahr, D. H., & Zysset, P. K. (2008). Influence of boundary conditions on computed apparent elastic properties of cancellous bone. *Biomechanics and Modeling in Mechanobiology*, 7(6), 463–476. <https://doi.org/10.1007/s10237-007-0109-7>

Patte, C., Brillet, P.-Y., Fetita, C., Gille, T., Bernaudin, J.-F., Nunes, H., Chapelle, D., & Genet, M. (2021). Estimation of regional pulmonary compliance in IPF based on personalized lung poromechanical modeling. *Submitted*.

Patte, C., Genet, M., & Chapelle, D. (2020). A poromechanical model of the lungs. *To be submitted*.

Patte, C., Genet, M., Fetita, C., Brillet, P.-Y., & Chapelle, D. (2019). Mécanique pulmonaire personnalisée : modélisation et estimation - Application à la fibrose pulmonaire. *CSMA 2019 - 14ème Colloque National en Calcul des Structures*. <https://hal.archives-ouvertes.fr/hal-02068920>

Perić, D., De Souza Neto, E. A., Feijóo, R. A., Partovi, M., & Molina, A. J. (2011). On micro-to-macro transitions for multi-scale analysis of non-linear heterogeneous materials: Unified variational basis and finite element implementation. *International Journal for Numerical Methods in Engineering*, 87(1-5), 149–170. <https://doi.org/10.1002/nme.3014>

Perlman, C. E., & Wu, Y. (2014). In situ determination of alveolar septal strain, stress and effective Young's modulus: An experimental/computational approach. *American Journal of Physiology - Lung Cellular and Molecular Physiology*, 307(4), L302–L310. <https://doi.org/10.1152/ajplung.00106.2014>

Ponte Castañeda, P. (1991). The effective mechanical properties of nonlinear isotropic composites. *Journal of the Mechanics and Physics of Solids*, 39(1), 45–71. [https://doi.org/10.1016/0022-5096\(91\)90030-R](https://doi.org/10.1016/0022-5096(91)90030-R)

Rausch, S. M., Haberthür, D., Stampanoni, M., Schittny, J. C., & Wall, W. A. (2011). Local strain distribution in real three-dimensional alveolar geometries. *Annals of Biomedical Engineering*, 39(11), 2835–2843. <https://doi.org/10.1007/s10439-011-0328-z>

Roth, C. J., Yoshihara, L., & Wall, W. A. (2017). A simplified parametrised model for lung microstructures capable of mimicking realistic geometrical and mechanical properties. *Computers in Biology and Medicine*, 89, 104–114. <https://doi.org/10.1016/j.combiomed.2017.07.017>

Saeb, S., Steinmann, P., & Javili, A. (2016). Aspects of Computational Homogenization at Finite Deformations: A Unifying Review From Reuss' to Voigt's Bound. *Applied Mechanics Reviews*, 68(5). <https://doi.org/10.1115/1.4034024>

Sanchez-Palencia, E. (1980). *Non-Homogeneous Media and Vibration Theory*. Springer-Verlag Berlin Heidelberg. <https://doi.org/10.1007/3-540-10000-8>

- Sarabia-Vallejos, M. A., Zuñiga, M., & Hurtado, D. E. (2019). The role of three-dimensionality and alveolar pressure in the distribution and amplification of alveolar stresses. *Scientific Reports*, 9(1), 1–11. <https://doi.org/10.1038/s41598-019-45343-4>
- Selvadurai, A. P., & Suvorov, A. P. (2016). Coupled hydro-mechanical effects in a poro-hyperelastic material. *Journal of the Mechanics and Physics of Solids*, 91, 311–333. <https://doi.org/10.1016/j.jmps.2016.03.005>
- Shakoor, M., Buljac, A., Neggers, J., Hild, F., Morgeneyer, T. F., Helfen, L., Bernacki, M., & Bouchard, P. O. (2017). On the choice of boundary conditions for micromechanical simulations based on 3D imaging. *International Journal of Solids and Structures*, 112, 83–96. <https://doi.org/10.1016/j.ijsolstr.2017.02.018>
- Soutas-Little, R. (2009). History of continuum mechanics. In J. Merodio & G. Saccomandi (Eds.), *EOLSS-UNESCO Encyclopedia*. Paris, UNESCO. <http://www.eolss.net>
- Suquet, P. M. (1987). Elements of homogenization for inelastic solid mechanics. In E. Sanchez-Palencia & A. Zaoui (Eds.), *Homogenization techniques for composite media* (pp. 193–278). Springer-Verlag, Berlin. <https://doi.org/10.1038/72256>
- Tadmor, E. B., Miller, R. E., & Elliott, R. S. (2012). *Continuum mechanics and thermodynamics: From fundamental concepts to governing equations*. Cambridge University Press. <https://doi.org/10.1017/CBO9781139017657>
- Tawhai, M. H., & Lin, C. L. (2010). Image-based modeling of lung structure and function. *Journal of Magnetic Resonance Imaging*, 32(6), 1421–1431. <https://doi.org/10.1002/jmri.22382>
- Terada, K., Hori, M., Kyoya, T., & Kikuchi, N. (2000). Simulation of the multi-scale convergence in computational homogenization approaches. *International Journal of Solids and Structures*, 37(16), 2285–2311. [https://doi.org/10.1016/S0020-7683\(98\)00341-2](https://doi.org/10.1016/S0020-7683(98)00341-2)

- Vincent, P. G., Monerie, Y., & Suquet, P. (2009). Porous materials with two populations of voids under internal pressure: I. Instantaneous constitutive relations. *International Journal of Solids and Structures*, 46(3-4), 480–506. <https://doi.org/10.1016/j.ijsolstr.2008.09.003>
- Virtanen, P., Gommers, R., Oliphant, T. E., Haberland, M., Reddy, T., Cournapeau, D., Burovski, E., Peterson, P., Weckesser, W., Bright, J., van der Walt, S. J., Brett, M., Wilson, J., Millman, K. J., Mayorov, N., Nelson, A. R., Jones, E., Kern, R., Larson, E., ... Vázquez-Baeza, Y. (2020). SciPy 1.0: fundamental algorithms for scientific computing in Python. *Nature Methods*, 17arXiv 1907.10121, 261–272. <https://doi.org/10.1038/s41592-019-0686-2>
- Warren, W. E., & Kraynik, A. M. (1997). Linear elastic behavior of a low-density Kelvin foam with open cells. *Journal of Applied Mechanics*, 64(4)arXiv arXiv:1011.1669v3, 787–794. <https://doi.org/10.1115/1.2788983>
- West, J. (2012). *Respiratory physiology: the essentials* (9th). Lippincott Williams & Wilkins.
- Willis, J. R. (1981). Variational and related methods for the overall properties of composites. *Advances in Applied Mechanics*, 21, 1–78. [https://doi.org/10.1016/S0065-2156\(08\)70330-2](https://doi.org/10.1016/S0065-2156(08)70330-2)
- Yamabe, J., Matsumoto, T., & Nishimura, S. (2011). Application of acoustic emission method to detection of internal fracture of sealing rubber material by high-pressure hydrogen decompression. *Polymer Testing*, 30(1), 76–85. <https://doi.org/10.1016/j.polymeresting.2010.11.002>
- Youssef, S., Maire, E., & Gaertner, R. (2005). Finite element modelling of the actual structure of cellular materials determined by X-ray tomography. *Acta Materialia*, 53(3), 719–730. <https://doi.org/10.1016/j.actamat.2004.10.024>

APPENDICES

A. BALANCE OF ANGULAR MOMENTUM AND SYMMETRY OF $\bar{\mathbf{U}}$

Rigid body motions consist of translations and rotations; they are not related to the deformation of bodies and difficult the solution of mechanical problems. The existence of this type of movements is related to the loading and boundary conditions imposed; in particular, in this appendix rigid body rotations will be analyzed in the context of the pressure-driven formulation presented in Chapter 2. For the kinematic uniform boundary conditions (KUBC), the constraints on the fluctuation term $\tilde{\mathbf{u}}$ produce forces on $\partial\Omega_0^E$ that are capable of balancing the system, so the body cannot present rotations (nor translations). However, for the periodic (PBC) and uniform traction (SUBC) boundary conditions, if the external forces produce an angular momentum different from zero, an additional constraint is needed to prevent the system's rotation. In this thesis, this constraint consisted of enforcing the macroscopic strain $\bar{\mathbf{U}}$ to be symmetric. Then, this appendix's objective is to show that the symmetry of $\bar{\mathbf{U}}$ is related to the balance of angular momentum.

To establish the relation between the symmetry of $\bar{\mathbf{U}}$ and the angular momentum, here it will be proved that for the PBC and SUBC, if $\bar{\mathbf{U}}$ is not enforced to be symmetric, then the momentum produced by the external forces (due to the pore pressure and body forces, for example), must be zero. Note this is equivalent to say that with PBC and SUBC, if the external forces produce an angular momentum different from zero, then $\bar{\mathbf{U}}$ must be symmetric. First, we will not enforce $\bar{\mathbf{U}}$ to be symmetric, then using the equation of balance of angular momentum and the properties of PBC and SUBC, we will conclude that the momentum produced by external forces must be zero.

To start, we note that the integral of the first Piola-Kirchhoff stress tensor can be expressed as

$$\int_{\Omega_0^S} \bar{\mathbf{P}} dV = \int_{\partial\Omega_0^S} \bar{\mathbf{P}}\mathbf{N} \otimes \hat{\mathbf{X}} dS = \int_{\partial\Omega_0^E} \bar{\mathbf{P}}\mathbf{N} \otimes \hat{\mathbf{X}} dS - \int_{\partial\Omega_0^N} p_0 J \mathbf{F}^{-T} \mathbf{N} \otimes \hat{\mathbf{X}} dS, \quad (\text{A.1})$$

with $\partial\Omega_0^S = \partial\Omega_0^E \cup \partial\Omega_0^N$ and where we replaced $\bar{\mathbf{P}}\mathbf{N}$ by the traction due to the pore pressure p_0 on $\partial\Omega_0^N$, using Equation (2.11). Then, replacing (A.1) in the stationary condition

with respect to $\bar{\mathbf{U}}$, Equation (2.16) (which is the same as Equation (B.9), in the case with body force)

$$\left[\int_{\partial\Omega_0^E} \bar{\mathbf{P}}\mathbf{N} \otimes \hat{\mathbf{X}} dS \right] : \delta\bar{\mathbf{U}} = 0 \quad \forall \delta\bar{\mathbf{U}} \in M_3. \quad (\text{A.2})$$

Now, as we do not enforce $\bar{\mathbf{U}}$ to be symmetric, then $\bar{\mathbf{U}} \in M_3$ and from Equation (A.2)

$$\int_{\partial\Omega_0^E} \mathbf{T} \otimes \hat{\mathbf{X}} dS = \mathbf{0}, \quad (\text{A.3})$$

where $\mathbf{T} = \bar{\mathbf{P}}\mathbf{N}$.

Let \mathbf{M}_{ext} be the momentum produced by external forces, then from the balance of angular momentum

$$\int_{\partial\Omega_0^E} \mathbf{x} \times \mathbf{T} dS + \mathbf{M}_{\text{ext}} = \mathbf{0}, \quad (\text{A.4})$$

but we can express the current coordinates \mathbf{x} as a function of the reference coordinates \mathbf{X} and the displacement, $\mathbf{x} = \mathbf{X} + \bar{\mathbf{U}}\hat{\mathbf{X}} + \tilde{\mathbf{u}}$, then

$$\int_{\partial\Omega_0^E} \mathbf{X} \times \mathbf{T} dS + \int_{\partial\Omega_0^E} \bar{\mathbf{U}}\hat{\mathbf{X}} \times \mathbf{T} dS + \int_{\partial\Omega_0^E} \tilde{\mathbf{u}} \times \mathbf{T} dS + \mathbf{M}_{\text{ext}} = \mathbf{0}. \quad (\text{A.5})$$

Now, we will show that for the periodic boundary conditions, the first three terms vanish.

First, note that due to the traction anti-periodicity

$$\int_{\partial\Omega_0^E} \mathbf{X}_0 \times \mathbf{T} dS = \mathbf{X}_0 \times \int_{\partial\Omega_0^E} \mathbf{T} dS = \mathbf{0}, \quad (\text{A.6})$$

then, the first term can be expressed as

$$\int_{\partial\Omega_0^E} \mathbf{X} \times \mathbf{T} dS = \int_{\partial\Omega_0^E} (\mathbf{X} - \mathbf{X}_0) \times \mathbf{T} dS = \int_{\partial\Omega_0^E} \hat{\mathbf{X}} \times \mathbf{T} dS, \quad (\text{A.7})$$

which is equal to zero due to (A.3). For the second term, using index notation

$$\int_{\partial\Omega_0^E} \varepsilon_{ijk} \bar{U}_{im} \hat{X}_m T_j dS = \varepsilon_{ijk} \bar{U}_{im} \int_{\partial\Omega_0^E} \hat{X}_m T_j dS = 0, \quad (\text{A.8})$$

and we see that the last integral is zero due to (A.3). The third term is zero due to the periodicity of $\tilde{\mathbf{u}}$ and the anti-periodicity of \mathbf{T} .

The procedure for the SUBC is similar, note that assuming a periodic domain and using the uniform traction condition

$$\int_{\partial\Omega_0^E} \mathbf{X}_0 \times \mathbf{T} dS = \mathbf{X}_0 \times \int_{\partial\Omega_0^E} \mathbf{T} dS = \mathbf{X}_0 \times \boldsymbol{\lambda} \int_{\partial\Omega_0^E} \mathbf{N} dS = \mathbf{0}, \quad (\text{A.9})$$

where $\int_{\partial\Omega_0^E} \mathbf{N} dS = \mathbf{0}$ due to the assumption of a periodic domain. Then, as done for the PBC

$$\int_{\partial\Omega_0^E} \mathbf{X} \times \mathbf{T} dS = \int_{\partial\Omega_0^E} \hat{\mathbf{X}} \times \mathbf{T} dS = \mathbf{0}, \quad (\text{A.10})$$

where the second term is zero due to (A.3). In index notation, the third term is rewritten using the uniform traction condition

$$\int_{\partial\Omega_0^E} \varepsilon_{ijk} \tilde{u}_i T_j dS = \int_{\partial\Omega_0^E} \varepsilon_{ijk} \tilde{u}_i \lambda_{jm} N_m dS = \varepsilon_{ijk} \lambda_{jm} \int_{\partial\Omega_0^E} \tilde{u}_i N_m dS = 0, \quad (\text{A.11})$$

where the last integral is zero due to the definition of $\mathcal{V}_i^{\text{subc}}$, Equation (2.31).

As the three first terms of Equation (A.5) are zero for the PBC and SUBC, the balance of angular momentum states

$$\mathbf{M}_{\text{ext}} = \mathbf{0}, \quad (\text{A.12})$$

i.e., the moment produced by the external forces must be zero.

B. MICROMECHANICAL ANALYSIS INCLUDING BODY FORCE

Suppose that, in addition to the pore pressure, a body force is present in the micromechanical analysis. In that case, the force equilibrium in the RVE requires special attention because the external forces are likely to be not self-equilibrated, and additional constraints may be needed. The most common example of a body force is gravity loading, in which case the external potential energy is

$$\Pi_{\text{ext}}(\bar{\mathbf{U}}, \tilde{\mathbf{u}}) = \int_{\Omega_0^S} \rho_0 \mathbf{g} \cdot (\bar{\mathbf{U}} \hat{\mathbf{X}} + \tilde{\mathbf{u}}) dV + p_0 V^F, \quad (\text{B.1})$$

where ρ_0 is the density of the solid in the reference configuration, \mathbf{g} is the acceleration due to gravity, and p_0 is the pore pressure.

Following a similar procedure as in the case without body force, the stationary condition of $\tilde{\mathbf{u}}$ yields

$$\begin{aligned} D_{\delta\tilde{\mathbf{u}}} \Pi_{\text{tot}}(\bar{\mathbf{U}}, \tilde{\mathbf{u}}, p) &= \int_{\partial\Omega_0^E} \bar{\mathbf{P}} \mathbf{N} \cdot \delta\tilde{\mathbf{u}} dS - \int_{\Omega_0^S} (\nabla_0 \cdot \bar{\mathbf{P}} + \rho_0 \mathbf{g}) \cdot \delta\tilde{\mathbf{u}} dV \\ &+ \int_{\partial\Omega_0^N} (\bar{\mathbf{P}} \mathbf{N} + p_0 J \mathbf{F}^{-T} \mathbf{N}) \cdot \delta\tilde{\mathbf{u}} dS = 0 \quad \forall \delta\tilde{\mathbf{u}} \in \mathcal{V}_{\tilde{\mathbf{u}}}. \end{aligned} \quad (\text{B.2})$$

Which is analogous to Equation (2.8), but incorporating the term $\rho_0 \mathbf{g}$. Then, in the strong form the last equation implies

$$\nabla_0 \cdot \bar{\mathbf{P}} + \rho_0 \mathbf{g} = \mathbf{0} \quad \text{in } \Omega_0^S, \quad (\text{B.3})$$

$$\bar{\mathbf{P}} \mathbf{N} = -p_0 J \mathbf{F}^{-T} \mathbf{N} \quad \text{on } \partial\Omega_0^N. \quad (\text{B.4})$$

The missing relation for $\partial\Omega_0^E$ depends on the kinematical constraint for $\tilde{\mathbf{u}}$, and as it does not depend on the external loads, its analysis is equivalent to the one performed in Section 2.2.1.

The stationarity with respect to \bar{U} yields

$$\begin{aligned} D_{\delta\bar{U}}\Pi_{\text{tot}}(\bar{U}, \tilde{\mathbf{u}}, p) &= \int_{\Omega_0^S} \bar{\mathbf{P}} : \nabla_0(\delta\bar{U} \hat{\mathbf{X}}) dV - \int_{\Omega_0^S} \rho_0 \mathbf{g} \cdot \delta\bar{U} \hat{\mathbf{X}} dV \\ &+ \int_{\partial\Omega_0^N} p_0 J \mathbf{F}^{-T} \mathbf{N} \cdot \delta\bar{U} \hat{\mathbf{X}} dS = 0 \quad \forall \delta\bar{U} \in \mathcal{V}_{\bar{U}}, \end{aligned} \quad (\text{B.5})$$

and as $\delta\bar{U}$ does not depend on \mathbf{X} ,

$$\begin{aligned} D_{\delta\bar{U}}\Pi_{\text{tot}}(\bar{U}, \tilde{\mathbf{u}}, p) &= \left[\int_{\Omega_0^S} \bar{\mathbf{P}} dV - \int_{\Omega_0^S} \rho_0 \mathbf{g} \otimes \hat{\mathbf{X}} dV \right. \\ &\left. + \int_{\partial\Omega_0^N} p_0 J \mathbf{F}^{-T} \mathbf{N} \otimes \hat{\mathbf{X}} dS \right] : \delta\bar{U} = 0 \quad \forall \delta\bar{U} \in \mathcal{V}_{\bar{U}}. \end{aligned} \quad (\text{B.6})$$

Using that $\hat{\mathbf{X}} = \mathbf{X} - \mathbf{X}_0$, and if \mathbf{X}_0 is the centroid of the solid

$$\int_{\Omega_0^S} \hat{\mathbf{X}} dV = \int_{\Omega_0^S} \mathbf{X} dV - \mathbf{X}_0 |\Omega_0^S| = 0, \quad (\text{B.7})$$

so, if $(\rho_0 \mathbf{g})$ is constant

$$\int_{\Omega_0^S} \rho_0 \mathbf{g} \otimes \hat{\mathbf{X}} dV = \rho_0 \mathbf{g} \otimes \int_{\Omega_0^S} \hat{\mathbf{X}} dV = \mathbf{0}. \quad (\text{B.8})$$

With this result, and in terms of the macroscopic stress $\langle \bar{\mathbf{P}} \rangle$, the Equation (B.6) can be rewritten as

$$\left[|\Omega_0^S| \langle \bar{\mathbf{P}} \rangle + \int_{\partial\Omega_0^N} p_0 J \mathbf{F}^{-T} \mathbf{N} \otimes \hat{\mathbf{X}} dS \right] : \delta\bar{U} = 0 \quad \forall \delta\bar{U} \in \mathcal{V}_{\bar{U}}, \quad (\text{B.9})$$

where it is interestingly to note that if \mathbf{X}_0 is the centroid of the solid, then Equation (B.9) is equal to the case without body forces. In summary, when the body force is added the only term in the strong form of the problem that varies is the differential equilibrium $\nabla_0 \cdot \bar{\mathbf{P}} + \rho_0 \mathbf{g} = \mathbf{0}$ in Ω_0^S .

When the gravity is included, the resultant force of external forces is likely to be different from zero, and the traction $\bar{\mathbf{P}} \mathbf{N}$ on the external boundary $\partial\Omega_0^E$ must balances the

system, i.e.

$$\int_{\partial\Omega_0^E} \bar{\mathbf{P}}\mathbf{N} \, dS - \int_{\partial\Omega_0^N} p_0 J \mathbf{F}^{-T} \mathbf{N} \, dS + \int_{\Omega_0^S} \rho_0 \mathbf{g} \, dV = \mathbf{0}, \quad (\text{B.10})$$

where the second plus the third term is the resultant of the external forces, that is assumed to be different from zero. In the KUBC case, as the fluctuation field $\tilde{\mathbf{u}}$ vanishes on the external boundary, the traction on $\partial\Omega_0^E$ will balance the system. However, as in the periodic case (PBC) the traction is anti-periodic

$$\int_{\partial\Omega_0^E} \bar{\mathbf{P}}\mathbf{N} \, dS = \mathbf{0}, \quad (\text{B.11})$$

and the sum of external forces must be zero. So, to handle the case where the body force and the pore pressure produce a non-zero total force, an additional constraint is needed. A straightforward option is to fix a random point; however, the solution would be highly dependent on this point. So, to reduce the arbitrariness of the solution, a Lagrange multiplier $\mathbf{s} \in \mathbb{R}^3$ can be used to enforce the average of $\tilde{\mathbf{u}}$ to be equal to zero in $\partial\Omega_0^E$, adding the following term in the potential energy of external forces

$$\Pi_{\text{ext},\mathbf{s}}(\tilde{\mathbf{u}}, \mathbf{s}) = \mathbf{s} \cdot \int_{\partial\Omega_0^E} \tilde{\mathbf{u}} \, dS, \quad (\text{B.12})$$

then,

$$\begin{aligned} D_{\delta\tilde{\mathbf{u}}}\Pi_{\text{tot}}(\bar{\mathbf{U}}, \tilde{\mathbf{u}}, p, \mathbf{s}) &= \int_{\partial\Omega_0^E} (\bar{\mathbf{P}}\mathbf{N} - \mathbf{s}) \cdot \delta\tilde{\mathbf{u}} \, dS + \int_{\partial\Omega_0^N} (\bar{\mathbf{P}}\mathbf{N} + p_0 J \mathbf{F}^{-T} \mathbf{N}) \cdot \delta\tilde{\mathbf{u}} \, dS \\ &\quad - \int_{\Omega_0^S} (\nabla_0 \cdot \bar{\mathbf{P}} + \rho_0 \mathbf{g}) \cdot \delta\tilde{\mathbf{u}} \, dV = 0 \quad \forall \delta\tilde{\mathbf{u}} \in \mathcal{V}_{\tilde{\mathbf{u}}}, \end{aligned} \quad (\text{B.13})$$

which implies Equations (B.3), (B.4) and additionally

$$(\bar{\mathbf{P}}\mathbf{N} - \mathbf{s})^+ = -(\bar{\mathbf{P}}\mathbf{N} - \mathbf{s})^- \quad \text{on } \partial\Omega_0^E. \quad (\text{B.14})$$

The stationarity with respect to $\delta\mathbf{s}$ yields

$$D_{\delta\mathbf{s}}\Pi_{\text{tot}}(\bar{\mathbf{U}}, \tilde{\mathbf{u}}, p, \mathbf{s}) = -\delta\mathbf{s} \cdot \int_{\partial\Omega_0^E} \tilde{\mathbf{u}} \, dS = 0 \quad \forall \delta\mathbf{s} \in \mathcal{V}_{\mathbf{s}}, \quad (\text{B.15})$$

with $\mathcal{V}_s = V_3$, where V_n is the space of all vectors in \mathbb{R}^n . Then,

$$\int_{\partial\Omega_0^E} \tilde{\mathbf{u}} \, dS = \mathbf{0}, \quad (\text{B.16})$$

so we define

$$\mathcal{V}_{\tilde{\mathbf{u}}}^{\text{pbcs}} := \{ \tilde{\mathbf{u}} \in H^1(\Omega_0^S) \mid \tilde{\mathbf{u}}(\mathbf{X}^+) = \tilde{\mathbf{u}}(\mathbf{X}^-) \ \forall \text{ pairs } \{ \mathbf{X}^+, \mathbf{X}^- \} \text{ and } \int_{\partial\Omega_0^E} \tilde{\mathbf{u}} \, dS = \mathbf{0} \}. \quad (\text{B.17})$$

And the strong form of the problem is similar to the periodic case, except for the definition of $\mathcal{V}_{\tilde{\mathbf{u}}}$ and the anti-periodic traction in $\partial\Omega_0^E$, which in this case is given by (B.14).

Note: From Equation (B.13) it can also be seen that,

$$\int_{\partial\Omega_0^E} (\bar{\mathbf{P}}\mathbf{N} - \mathbf{s}) \, dS = \mathbf{0}, \quad (\text{B.18})$$

so,

$$\mathbf{s} |\partial\Omega_0^E| = \int_{\partial\Omega_0^E} \bar{\mathbf{P}}\mathbf{N} \, dS, \quad (\text{B.19})$$

with $|\partial\Omega_0^E|$ the area of $\partial\Omega_0^E$. Then, (B.19) in (B.10)

$$\mathbf{s} = \frac{1}{|\partial\Omega_0^E|} \left(\int_{\partial\Omega_0^N} p_0 J \mathbf{F}^{-T} \mathbf{N} \, dS - \int_{\Omega_0^S} \rho_0 \mathbf{g} \, dV \right), \quad (\text{B.20})$$

which means that \mathbf{s} can be interpreted as a traction in the boundary $\partial\Omega_0^E$ that balances the system.

For the uniform traction condition (SUBC), if the RVE is periodic

$$\int_{\partial\Omega_0^E} \bar{\mathbf{P}}\mathbf{N} \, dS = \int_{\partial\Omega_0^E} \boldsymbol{\lambda}\mathbf{N} \, dS = \boldsymbol{\lambda} \int_{\partial\Omega_0^E} \mathbf{N} \, dS = \mathbf{0}, \quad (\text{B.21})$$

where $\bar{\mathbf{P}}\mathbf{N} = \boldsymbol{\lambda}\mathbf{N}$ is the uniform traction condition, and the integral of \mathbf{N} on the external boundary is zero due to its anti-periodicity. Therefore, if the external forces produce a non-zero total force, an additional constraint is needed, that analogously to the PBC, can be, for example, fix a random point or include the mentioned Lagrange multiplier \mathbf{s} . Moreover, with the SUBC the fluctuation term can have rigid body rotations, so additional constraints

are needed, as detailed by Javili et al. (2017). Note that as the rotations are not periodic, they cannot occur with the PBC.

C. MACROSCOPIC AVERAGED RESPONSE

With the macroscopic strain \bar{U} obtained from the pressure-driven simulation, we compute a macroscopic deformation gradient tensor: $\mathbf{F}^c = \mathbf{I} + \nabla_0(\bar{U} \hat{\mathbf{X}}) = \mathbf{I} + \bar{U}$, and we plot its determinant in Figure C.1. For both spherical and image-based alveolar models, the stiffest response is given by KUBC, followed by PBC and SUBC, which gives the most compliant. For the KUBC the results are similar for the spherical and image-based models, while for the PBC and SUBC, the strain levels are higher in the spherical alveolar model.

The macroscopic Cauchy stress tensor in the solid is defined as

$$\langle \boldsymbol{\sigma} \rangle := \frac{1}{|\Omega^S|} \int_{\Omega^S} \boldsymbol{\sigma} \, dv, \quad (\text{C.1})$$

and we plot its hydrostatic and von Mises components in Figure C.2. The results show that the hydrostatic stress is different for both models; the spherical geometry gives positive values with a maximum of approximately 3 kPa (with slight differences depending on the kinematical constraints), while the image-based model gives negative values, with a response that is indistinguishable between the different kinematical constraints. Regarding the von Mises stress, it is zero with the spherical alveolar model, while the image-based model gives values with a maximum between 0.4 and 0.5 kPa.

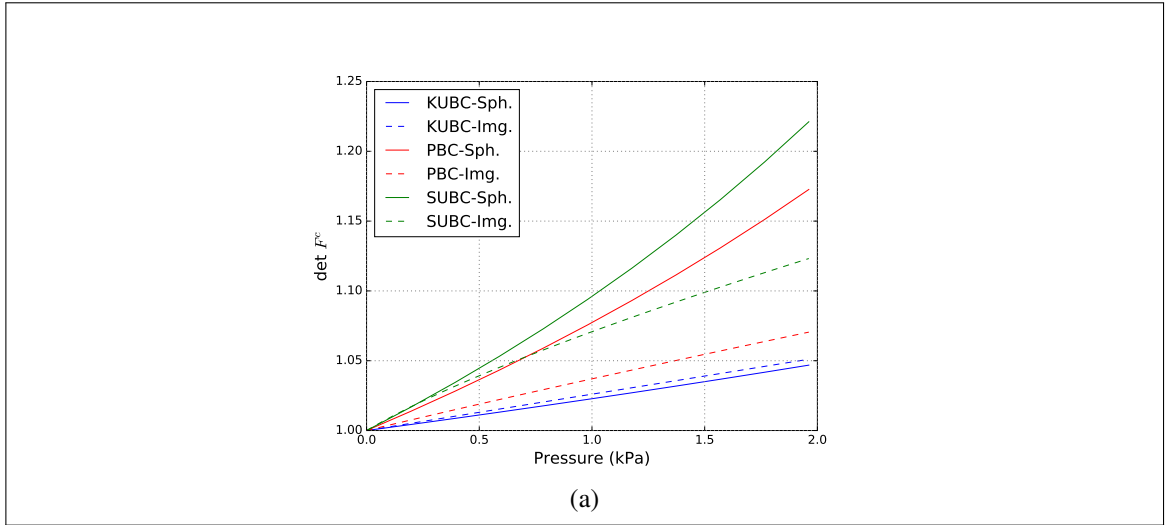


Figure C.1. To quantify the macroscopic deformation with the spherical alveolar model (continuous lines) and the image-based alveolar model (dashed lines), the determinant of F^c is shown for the different kinematical constraints studied: KUBC (blue), PBC (red) and SUBC (green). In both cases, KUBC gives the stiffest response, PBC an intermediate value, and SUBC the most compliant.

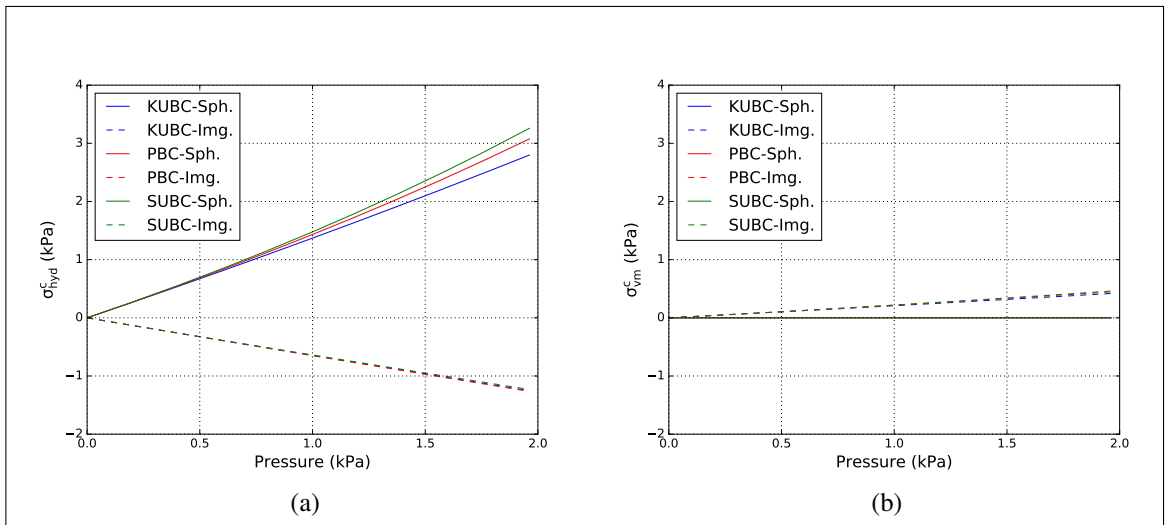


Figure C.2. (a) Hydrostatic and (b) von Mises components of the macroscopic Cauchy stress in the solid, for the spherical alveolar model (continuous lines) and image-based alveolar model (dashed lines), in the pressure-driven case. The colors indicate the different kinematical constraints studied: KUBC (blue), PBC (red), and SUBC (green).